APPLICATION OF LARGE EDDY SIMULATION TO COOLING AND FLOW PROBLEMS IN AEROPROPULSION SYSTEMS

Richard H. Pletcher
Kunlun Liu
Zhaohui Qin
Joon Lee

Department of Mechanical Engineering
Iowa State University
Ames, Iowa 50011

September 29, 2004

The views and conclusions contained herein are those of the authors and should not be interpreted as necessarily representing the official policies or endorsements, either expressed or implied, of the Air Force Office of Scientific Research or the U. S. Government.

REPORT DOCUMENTATION PAGE

AFRL-SR-AR-TR-04-

0524

1. REPORT DATE *(DD-MM-YYYY)*	2. REPORT TYPE	3. DATES COVERED *(From - To)*
29-09-2004	Final	1 January 2001-30 June 2004

4. TITLE AND SUBTITLE	5a. CONTRACT NUMBER
Application of Large Eddy Simulation to Cooling and Flow Problems in Aeropropulsion Systems	5b. GRANT NUMBER AFOSR F49620-01-1-0113
	5c. PROGRAM ELEMENT NUMBER

6. AUTHOR(S)	5d. PROJECT NUMBER
Richard H. Pletcher, Kunlun Liu, Zhaohui Qin, Joon Lee	5e. TASK NUMBER
	5f. WORK UNIT NUMBER

7. PERFORMING ORGANIZATION NAME(S) AND ADDRESS(ES)	8. PERFORMING ORGANIZATION REPORT NUMBER
Department of Mechanical Engineering Black Engineering Building Iowa State University Ames, Iowa 50011	ISU-MEP-CFD-0904

9. SPONSORING / MONITORING AGENCY NAME(S) AND ADDRESS(ES)	10. SPONSOR/MONITOR'S ACRONYM(S)
Air Force Office of Scientific Research/NA Turbulence and Rotating Flows 4015 Wilson Blvd. Room 713 Arlington VA 22203	AFOSR
	11. SPONSOR/MONITOR'S REPORT NUMBER(S)

12. DISTRIBUTION / AVAILABILITY STATEMENT
Approved for public release; distribution unlimited

13. SUPPLEMENTARY NOTES

14. ABSTRACT
The primary objective of this research was to develop and apply large eddy simulation (LES) technology to some urgent flow and heat transfer problems in propulsion systems and to contribute to the physical understanding of such flows. The work was motivated by the observation that the design goals of high specific power and thrust and low specific fuel consumption have been reached, in part, by an increase in turbine inlet temperature and future improvements in engine efficiency will place even greater demands on blade cooling procedures. However, current design codes are somewhat limited in accuracy due to uncertainty associated with modeling for turbulent flow. The research was concerned with both the film cooling of external blade surfaces and the complex flows in internal cooling passages. Studies have been completed of the effects of rotation on the heat transfer and flow in smooth and ribbed channels and in a duct of square cross-section. A scheme was developed for including the effects of freestream turbulence on boundary layer development. Preliminary LES results have been obtained for a single hole film cooling configuration.

15. SUBJECT TERMS
Large eddy simulation, turbulent flow, heat transfer, turbine cooling

16. SECURITY CLASSIFICATION OF:			17. LIMITATION OF ABSTRACT	18. NUMBER OF PAGES	19a. NAME OF RESPONSIBLE PERSON
a. REPORT	b. ABSTRACT	c. THIS PAGE	UL	i-xii,	19b. TELEPHONE NUMBER *(include area code)*
Unclassified	Unclassified	Unclassified		1-92	

Standard Form 298 (Rev. 8-98)
Prescribed by ANSI Std. Z39.18

i

Contents

List of Figures

List of Tables

Nomenclature

Roman Symbols

$[A],[B],[C]$	inviscid flux Jacobians
$\mathbf{B}$	body force vector
$\mathbf{C}$	discretized convective and viscous flux vector
C_d, C_i	dynamic subgrid-scale model coefficients
C_{ij}	cross subgrid-scale stress tensor
C_f	friction coefficient $(= 2\tau_w / (\rho_{ref} U_{ref}^2))$
c	speed of sound $(= \sqrt{\gamma R T})$
C_p	constant pressure specific heat, coefficient of pressure
C_v	constant volume specific heat
D	diameter of pipe
D_h	hydraulic diameter
E	specific energy
$\mathbf{E}, \mathbf{F}, \mathbf{G}$	flux vectors
e	specific internal energy $(= C_v T)$
G	filter function
G_r	Grashof number $(= (g D_h^4 q_w) / (v_b^2 k_b T_b))$
g	gravitational constant
H	total enthalpy $(= h + u_i u_i / 2)$
H_j	resolved turbulent heat flux vector
h	heat transfer coefficient, or specific enthalpy
$\vec{i}, \vec{j}, \vec{k}$	unit vectors for Cartesian coordinate system
k	wave number, thermal conductivity, or turbulent kinetic energy
$[L], [D], [U]$	approximate factorization matrices for LU-SGS scheme
L_{ij}	Leonard subgrid-scale stress tensor
L_{ref}	reference length
L_x	streamwise length
M	Mach number

m	pseudo time index
$\dot{m}$	dimensionless mass flow rate
N_{stat}	number of time steps for turbulent statistics
Nu_D	Nusselt number based on hydraulic diameter $(= hD_h/k_b)$
n	physical time index
ni, nj, nk	control volume numbers in streamwise, wall normal and spanwise (circumferential) directions
$\vec{n}$	unit normal vector
n_x, n_y, n_z	components of unit normal vector
Pr	Prandtl number $(= \mu c_p/k)$
Pr_t	turbulent Prandtl number
p	thermodynamic pressure
Q_j	subgrid-scale turbulent heat flux vector
Q_{tj}	test filtered heat flux vector
q_j	heat flux vector
q_{tj}	Favre filtered heat flux vector
q_w	nondimensional wall heat flux
R	gas constant
R_{ij}	Reynolds subgrid-scale stress tensor
$\mathbf{R}$	residual vector
r	radius of pipe
$\mathfrak{R}$	preconditioned residual vector
Ra	Rayleigh number
Re	generic Reynolds number
Re_D	bulk Re based on hydraulic diameter $(= \rho_b u_b D_h/\mu_b)$
Re_{ref}	Re based on reference quantities $(= \rho_{ref} V_{ref} L_{ref}/\mu_{ref})$
Re_τ	Reynolds number based on friction velocity $(= \rho_{ref} u_\tau D/\mu_{ref})$
Re_δ	bulk Re based on half-distance between inner wall and outer wall
S	magnitude of cell face area vector or skewness factor
$\vec{S}$	cell face area vector

S_{ij}	strain rate tensor
T	thermodynamic temperature
T_b	bulk temperature
$[T]$	time derivative Jacobian $(= \partial \mathbf{W}/\partial \mathbf{U})$
TKE	turbulent kinetic energy
T_τ	friction temperature $(= q_w / (\rho_w C_p u_\tau))$
T_w	wall temperature
T_{ij}	test filtered stress tensor
t	physical time
$[U]$	vector of conserved variables $[\rho, \rho u, \rho v, \rho w, \rho E]^T$
u_τ	friction velocity $(= \sqrt{\tau_w/\rho_w})$
u_τ^*	semi-local friction velocity $(= \sqrt{\tau_w/\rho(y)})$
u, v, w	Cartesian velocity components in x, y, z directions
u, u_r, u_θ	Cylindrical velocity components
u^+	velocity in wall coordinates $(= u/u_\tau)$
u^*	velocity in semi-local coordinates $(= u/u_\tau^*)$
V_r	reference velocity
$\mathbf{W}$	vector of primitive variables $[p, u, v, w, T]^T$
x, y, z	Cartesian coordinates
y^+	distance to wall in wall coordinates
y^*	distance to wall in semi-local coordinates

Greek Symbols

α, π, ε	subgrid-scale terms in energy equation
β	pressure gradient parameter
Γ	time derivative preconditioning matrix
γ	ratio of specific heats
Δ	grid filter width

$\hat{\Delta}$	test filter width
δ	half distance between inner and outer wall of annular pipe or Kronecker delta
δ_y	distance to closest wall
θ	temperature difference $(= T_w - T)$ or circumferential direction of pipe
θ^+	temperature in wall coordinates $(= \theta/T_\tau)$
κ	von Karman constant
λ	eigenvalue
μ	molecular dynamic viscosity
μ_t	subgrid-scale turbulent viscosity
ν	molecular kinematic viscosity $(= \mu/\rho)$
ν_t	subgrid-scale turbulent kinematic viscosity $(= \mu_t/\rho)$
ρ	thermodynamic density
σ_{ij}	shear stress tensor
τ	pseudo time
τ_{ij}	subgrid-scale stress tensor
Φ	temperature gradient parameter
Ω	cell volume

Subscripts

b	bulk property
g	ghost cell quantity
i,j,k	indices for Cartesian coordinates
inv	inviscid contribution
nb	near wall cell quantity
p	periodic component
ref	reference quantity
res	resolved contribution
rms	root-mean-square

s or *sgs*	subgrid-scale contribution
v or *vis*	viscous contribution
w	wall value
x,y,z	associated with Cartesian direction
β	cell face index
θ	associated with circumferential direction of pipe

Superscripts and Other Symbols

$*$	dimensional variable or semi-local coordinates
$\star$	dimensional variable
$+$	wall coordinates
$'$	fluctuation with respect to ensemble average, or unresolved or subgrid-scale component of filtered quantity
$''$	fluctuation with respect to Favre ensemble average, or unresolved or subgrid-scale component of Favre filtered quantity
$\rightarrow$	vector quantity
$-$	resolved or large scale component of filtered quantity
$\sim$	resolved or large scale component of Favre filtered quantity
$\frown$	test filtered quantity
$<>$	ensemble averaged quantity
$<>_s$	ensemble averaged in streamwise and circumferential directions

Abstract

The primary objective of this research was to develop and apply large eddy simulation (LES) technology to some urgent flow and heat transfer problems in propulsion systems and to contribute to the physical understanding of such flows. The work was motivated by the observation that the design goals of high specific power and thrust and low specific fuel consumption have been reached, in part, by an increase in turbine inlet temperature and future improvements in engine efficiency will place even greater demands on blade cooling procedures. However, current design codes are somewhat limited in accuracy due to uncertainty associated with modeling for turbulent flow. The research was concerned with both the film cooling of external blade surfaces and the complex flows in internal cooling passages. Studies have been completed showing the effects of rotation on the heat transfer and flow in smooth and ribbed channels and in a duct of square cross-section. A scheme was developed for including the effects of freestream turbulence on boundary layer development. Preliminary LES results have been obtained for a single hole film cooling configuration.

1 Introduction

This report summarizes the research accomplishments achieved under Grant AFOSR F49620-01-1-0113, "Application of Large Eddy Simulation to Cooling and Flow Problems in Aeropropulsion Systems." The objective of the research was to expand the capabilities of LES technology to contribute to the solution of urgent problems in propulsion systems and to contribute to the physical understanding of such flows. The long-term goal of the thrust is to advance large eddy simulation (LES) technology to the point where it is effective for computing realistic flows in a rotating, multistage turbomachine. First, however, some building block simulations need to be carried out for a single blade element.

Flows in propulsion systems are accompanied by effects such as rotation and high turbulence levels that alter the basic structure of turbulent flows in ways that are not accurately represented by current design codes that rely heavily on turbulence models. Significant improvements in efficiency can be achieved if the uncertainty associated with design predictions can be reduced. As computer technology continues to advance, it is anticipated that large eddy simulation (LES) in which turbulence modeling plays a minor part will play an ever-increasing role in the understanding of such complex flows and will enable preliminary design decisions to be based on more accurate computational models. Turbine cooling issues have become very important since the design goals of high specific power and thrust and low specific fuel consumption have been reached, in part, by an increase in turbine inlet temperature. Future improvements in engine efficiency will place even greater demands on blade cooling procedures. Accordingly, the the research has focused on developing and applying large eddy simulation (LES) technology to idealized configurations for both the film cooling of external blade surfaces and the complex flows in internal cooling passages.

Large eddy simulation uses large computer resources but is capable of achieving very realistic results because very little ad hoc modeling is employed to represent the effects of turbulence. The unsteady, three-dimensional motion of the large eddies is resolved from first principles and modeling is only used to account for the effects of eddies smaller than the computational grid itself. Such small eddies tend to be nearly isotropic and universal. The role of LES in dealing with propulsion technology is two fold. First, the technique can be used to supplement the fundamental information obtained from experiments in that effects not easily established experimentally such as large tem-

1

perature differences, heat flux levels and rotation effects can be imposed in the simulations. Second, LES has the potential to become a valuable predictive tool for practical turbulent flows as computer technology continues to advance. For this to occur, however, considerable work is required to find innovative ways of simulating flows at higher Reynolds numbers, computationally efficient ways of accommodating geometries of increasing complexity, and for implementing general inflow and outflow conditions.

The numerical formulation used in the research is based on a finite volume discretization of the Favre-filtered compressible Navier-Stokes equations. Significant levels of heat transfer occur in the gas flows of interest and the compressible formulation enables the effects of property variations to be taken into account. The scheme solves for the primitive variables of velocity, pressure, and temperature in a fully coupled manner. The results reported here employed a modified version of the LU-SGS implicit scheme [1, 2] that has been optimized for parallel implementation using the message-passing interface (MPI). Low Mach number preconditioning [3] was used to enable solutions to be obtained efficiently at the low Mach numbers arising in many applications of interest. A dynamic subgrid-scale model has been used in all simulations reported here.

Facets of the research have included:

- Channel flows with rotation and with and without ribs

- Square duct flows with rotation

- Algorithm developments including ways to develop inflow conditions for the turbulent boundary layer

- The effects of freestream turbulence on turbulent boundary characteristics

- Film cooling

The organization of this report is as follows. First the conservation equations will be presented in a general form that served as a starting point for development of the various specific forms needed to address the several applications listed above. Next the application areas will be discussed in the order, rotating channel flows, internal passage flows including effects of rotation and centrifugal buoyancy, turbulent boundary layer flows developing under the influence of freestream turbulence, and film cooling flows. The additions and changes needed to specialize the conservation principles

2

for each application will be explained in the separate sections devoted to that applications. Likewise, relevant numerical details will given as the application areas are discussed.

2   Governing Equations–General

In this report, flow variables are nondimensionlized as follows,

$$x_i = \frac{x_i^*}{L_{ref}} \qquad u_i = \frac{u_i^*}{U_{ref}} \qquad t = \frac{t^*}{(L_{ref}/U_{ref})} \qquad \rho = \frac{\rho^*}{\rho_{ref}}$$

$$p = \frac{p^*}{\rho_{ref}U_{ref}^2} \qquad T = \frac{T^*}{T_{ref}} \qquad e = \frac{e^*}{U_{ref}^2} \qquad \mu = \frac{\mu^*}{\mu_{ref}} \tag{1}$$

$$k = \frac{k^*}{k_{ref}} \quad c_v = \frac{c_v^*}{(U_{ref}^2/T_{ref})} \quad R = \frac{R^*}{(U_{ref}^2/T_{ref})} \quad c_p = \frac{c_p^*}{(U_{ref}^2/T_{ref})}$$

where the dimensional variables have been denoted with a superscript asterisk. The reference Mach number is $M_{ref} = U_{ref}/\sqrt{\gamma R^* T_{ref}}$. The fluid is assumed to be an ideal gas and the non-dimensional equation of state is $p = \rho RT$. The non-dimensional coefficients of viscosity and thermal conductivity were evaluated as: $\mu = k = T^a$ where a is assumed to be 0.71. The specific heats and molecular Prandtl number were treated as constants.

In compressible flow, fluid properties may vary temporally and spatially due to the simultaneous fluctuations in dilatation, heat transfer and momentum transfer. A mass-weighted averaging is recommended for properties carried by fluid elements which are related to mass conservation. Favre-filtering [21] was utilized for this purpose. Consequently, the Favre-filtered compressible Navier-Stokes equations are

$$\frac{\partial \overline{\rho}}{\partial t} + \frac{\partial (\overline{\rho}\tilde{u}_j)}{\partial x_j} = 0 \tag{2}$$

$$\frac{\partial (\overline{\rho}\tilde{u}_i)}{\partial t} + \frac{\partial (\overline{\rho}\tilde{u}_i\tilde{u}_j)}{\partial x_j} = -\frac{\partial \overline{p}}{\partial x_i} + \frac{\partial \hat{\sigma}_{ij}}{\partial x_j} - \frac{\partial \tau_{ij}}{\partial x_j} \tag{3}$$

$$\frac{\partial (\overline{\rho}\hat{E})}{\partial t} + \frac{\partial [(\overline{\rho}\hat{E} + \overline{p})\tilde{u}_j]}{\partial x_j} = \frac{\partial (\tilde{u}_i\hat{\sigma}_{ij})}{\partial x_j} - \frac{\partial \tilde{q}_j}{\partial x_j} - \frac{\partial Q_j}{\partial x_j} - \gamma - \pi - \varepsilon \tag{4}$$

The overline, $\widetilde{\langle \bullet \rangle}$, denotes a Favre-filtered quantity. $\hat{E} = c_v\tilde{T} + \frac{1}{2}\tilde{u}_i\tilde{u}_j$, and $\hat{\sigma}_{ij} = \frac{2\overline{\mu}}{Re_r}(\tilde{S}_{ij} - \frac{1}{3}\tilde{S}_{kk}\delta_{ij})$. Moreover, the equation of state becomes

$$\overline{p} = R\overline{\rho}\tilde{T} \tag{5}$$

The effects of the small-scale motions are present in the above equations through the subgrid-scale

4

(SGS) stress tensor, τ_{ij}, in the momentum equation as

$$\tau_{ij} = \overline{\rho}(\widetilde{u_i u_j} - \tilde{u}_i \tilde{u}_j) \tag{6}$$

and the SGS terms that are the last four terms on the right hand side of Eq. (4) as

$$Q_j = \overline{\rho} c_v (\widetilde{T u_j} - \tilde{T} \tilde{u}_j) \tag{7}$$

$$\gamma = \tilde{u}_i \frac{\partial \tau_{ij}}{\partial x_j} \tag{8}$$

$$\pi = \overline{p \frac{\partial u_j}{\partial x_j}} - \overline{p} \frac{\partial \tilde{u}_j}{\partial x_j} \tag{9}$$

$$\varepsilon = \overline{\sigma_{ij} \frac{\partial u_i}{\partial x_j}} - \hat{\sigma}_{ij} \frac{\partial \tilde{u}_j}{\partial x_j} \tag{10}$$

where Q_j is the SGS heat flux vector. The terms γ, π and ε were neglected since only low Mach flows were considered [17].

The filtered dimensionless viscous stress and heat flux vectors were approximated by assuming that the correlations between the fluid properties and the derivatives of the velocity or temperature were weak [22]. The approximations are

$$\overline{\sigma}_{ij} \approx \hat{\sigma}_{ij} = \frac{2\overline{\mu}}{Re_{ref}} \left(\tilde{S}_{ij} - \frac{1}{3} \tilde{S}_{kk} \delta_{ij} \right) \tag{11}$$

and

$$\overline{q}_j \approx \hat{q}_j = -\frac{c_p \overline{\mu}}{Re_{ref} P_r} \frac{\partial \tilde{T}}{\partial x_j} \tag{12}$$

where the strain rate tensor is

$$\tilde{S}_{ij} = \frac{1}{2} \left(\frac{\partial \tilde{u}_i}{\partial x_j} + \frac{\partial \tilde{u}_j}{\partial x_i} \right) \tag{13}$$

To close the equations, the SGS stress tensor and heat flux vector in the Favre-filtered equations need be modeled. A dynamic model proposed for compressible turbulence by Moin et al. [7] and recommended by Lilly [23] was implemented.

5

The anisotropic part of the SGS stress tensor based on the grid filter was modeled as

$$\tau_{ij} - \frac{1}{3}\tau_{kk}\delta_{ij} = -2C_d\bar{\rho}\Delta^2|\tilde{S}|\left(\tilde{S}_{ij} - \frac{1}{3}\tilde{S}_{kk}\delta_{ij}\right) \tag{14}$$

And the isotropic part of SGS stress tensor, τ_{kk}, becomes

$$\tau_{kk} = 2C_I\bar{\rho}\Delta^2|\tilde{S}|^2 \tag{15}$$

The isotropic part of SGS stress tensor was neglected because it has a lower order of magnitude than the thermodynamic pressure [7]. The coefficient, C_d, was computed dynamically by

$$C_d = \frac{\langle L_{ij}M_{ij}\rangle}{\langle M_{kl}M_{kl}\rangle} \tag{16}$$

where

$$L_{ij} = \widehat{\bar{\rho}\tilde{u}_i\tilde{u}_j} - \frac{\widehat{\bar{\rho}\tilde{u}_i}\widehat{\bar{\rho}\tilde{u}_j}}{\hat{\bar{\rho}}} \tag{17}$$

$$M_{ij} = -2\hat{\bar{\rho}}\hat{\Delta}^2|\hat{\tilde{S}}|(\hat{\tilde{S}}_{ij} - \frac{1}{3}\hat{\tilde{S}}_{kk}\delta_{ij}) + 2\Delta^2\widehat{\bar{\rho}|\tilde{S}|(\tilde{S}_{ij} - \frac{1}{3}\tilde{S}_{kk}\delta_{ij})} \tag{18}$$

A procedure similar to the modeling of the SGS stress tensor was followed to represent the SGS heat flux vector. Considering the modeling for the eddy diffusivity SGS model, the subgrid-scale heat flux vector can be modeled as

$$\begin{aligned} Q_j &= -\frac{c_p\mu_t}{Pr_t}\frac{\partial \tilde{T}}{\partial x_j} \\ &= -\frac{c_pC_d\bar{\rho}\Delta^2|\tilde{S}|}{Pr_t}\frac{\partial \tilde{T}}{\partial x_j} \end{aligned} \tag{19}$$

where Pr_t is the turbulent Prandtl number and calculated dynamically as

$$Pr_t = -c_pC_d\frac{\langle F_jF_j\rangle}{\langle H_kF_k\rangle} \tag{20}$$

where

$$H_j = c_v\left(\widehat{\bar{\rho}\tilde{u}_j\tilde{T}} - \frac{\widehat{\bar{\rho}u_j}\widehat{\bar{\rho}T}}{\hat{\bar{\rho}}}\right) \tag{21}$$

$$F_j = \hat{\bar{\rho}}\hat{\Delta}^2|\hat{\tilde{S}}|\frac{\partial\hat{\tilde{T}}}{\partial x_j} - \Delta^2\left(\widehat{\bar{\rho}|\tilde{S}|\frac{\partial\tilde{T}}{\partial x_j}}\right) \qquad (22)$$

3 Channel Flows with Rotation

3.1 Introduction

Turbulent rotating flows are of considerable interest in a variety of industrial, geophysical and astrophysical applications. Examples are natural flows like ocean currents, estuaries and atmospheric boundary layers, and engineering flows in rotating devices such as turbines, pumps, compressors and cyclone separators. It is well known that system rotation affects both the mean motion and the turbulence statistics. Many rotational-induced flow phenomena have been reviewed by Tritton [4] and Hopfinger [5].

System rotation influences turbulence in several ways: for example, it may decrease energy transfer from large to small scales or reduce turbulence dissipation and the decay rate of turbulence energy. In rotating channel flow, system rotation can both stabilize and destabilize the flow. On the unstable side, Coriolis forces enhance turbulence production and increase the intensity of turbulence, while on the stable side, Coriolis forces reduce turbulence production and decrease the intensity of turbulence (Piomelli and Liu [6]).

Most large eddy simulations (LES) of flows with heat transfer reported to date employed an incompressible formulation and treated temperature as a passive scalar. However, compressible formulations have been employed in a few recent works (Moin et al. [7] and Dailey et al. [2]) where the coupling between velocity and temperature fields were considered.

Rotating channel flows have been investigated experimentally (Johnston [8]; Han et al. [9]) and numerically (Piomelli [6]; Kristofferson and Anderson [10]). However, very little information is available for rotating channel flow with heat transfer, especially from the LES or DNS community.

The flow over two and/or three-dimensional obstacles of different shapes and sizes with and without rotation have been studied extensively by numerous investigators due to its importance to engineering applications. Among these are flows in turbines, pumps, diffusers, and electronic components (Matsubara and Alfreson [11]). In many of these applications, enhanced surfaces and rotation significantly alter the structure of the turbulence. Han et al. [12] conducted an experimental study to investigate the effect of rib geometry on friction factor and Stanton number for turbulent flow. It was found that the shape of the rib affected the friction factor, while a modest effect was

observed on the heat transfer.

Bergeles and Athanassiadis [13] studied the influence of the streamwise length of a rib on reattachment length and showed that a sudden decrease in reattachment length from 11 to 3 rib heights was observed when the length to height ratio of a rib was greater than 4. Sparrow and Tao [14] used the naphthalene sublimation technique in flat rectangular channels of large aspect ratios with obstacles situated on one of the walls of the channel and oriented transversely to the flow direction. The results showed a substantial enhancement of Sherwood numbers (Sh) compared with the smooth-wall duct. Drain and Martin [15] performed laser doppler velocimetry(LDV) measurements of the fully developed water flow in a rectangular duct with one surface roughened with a periodic array of elements. They found that the k-ε turbulence model tended to seriously underestimate the reattachment length, which is an important indicator of turbulence structure.

According to Wagner et al. [16], approximately 75 % of the estimated uncertainty in calculating the heat transfer coefficient was due to the temperature measurement error. Furthermore, it can be very difficult and expensive to obtain detailed information about the flow distribution in a ribbed rotating passage experimentally. Large eddy simulation presents an attractive alternative to experiments for studying details of such flows. The goal of the present study was to perform a large eddy simulation of rotating turbulent flow in a plane channel with and without transverse square ribs on the walls. Periodic and step periodic (Dailey et al. [2]) boundary conditions were used at the inflow and outflow boundaries since fully developed channel flows were considered. This assumption allows the computed domain to be limited to the region between two adjacent ribs so that a reasonable computational grid can be used.

3.2 Numerical Method

In the present research, a compressible LES formulation was used, which also permited the subgrid-scale turbulent Prandtl number to be computed dynamically. A finite volume method was used to numerically solve the governing equations. The code used Cartesian hexahedral control volumes, and solved for the primitive variables (p, u, v, w, T) that were stored at the cell centers. Besides the physical time integration, pseudo time iterations were performed to resolve nonlinearities in the algebraic formulation and to implement the low Mach number preconditioning using an implicit LU-SGS scheme. The low Mach number preconditioning was used to enable the compress-

ible code to work efficiently at nearly incompressible speeds. The solver is second-order accurate in both space and time (Dailey and Pletcher [18]). The multiblock code was parallelized using the message passing interface (MPI). The computations were carried out on an IBM SP2 (Minnesota Supercomputing Institute) using 17 processors.

When property variations are taken into account, flows with heating or cooling do not attain a fully-developed state. However, experiments show that far downstream of the entry region, a slowly evolving quasi-developed state exists. Dailey and Pletcher [18] showed that a short section of the downstream region could be computed in a "stepwise periodic" manner with the following streamwise boundary conditions.

$$
\begin{aligned}
\rho u(0,y) &= \rho u(L_x,y) \\
v(0,y) &= v(L_x,y) \\
w(0,y) &= w(L_x,y) \\
p_P(0,y) &= p_P(L_x,y) \\
T(0,y) &= T(L_x,y) - \Delta T_x
\end{aligned}
\tag{23}
$$

where L_x is the length of the computation domain in the streamwise direction and $\bar{p}_P$ is the periodic component of the pressure $\bar{p}(x,y,z,t) = \beta x + \bar{p}_p(x,y,z,t)$, where β is the average streamwise pressure gradient. The temperature difference ΔT_x is computed from an energy balance utilizing the uniform heat flux imposed and the mass flux. All primitive variables $(\tilde{p}, \tilde{u}_i, \tilde{T})$ were assumed to be periodic in the spanwise (z) direction.

The conventional Reynolds (or ensemble) average of a quantity is denoted as $<>$, and the Favre ensemble average as $\{\}$, where

$$
\{f\} = < \rho f > / < \rho > .
\tag{24}
$$

A single prime $'$, and a double prime $''$, denote the turbulent fluctuations with respect to the Reynolds or Favre ensemble average, respectively.

The velocity fluctuations were obtained at each time step as

$$
\tilde{u}_i'(x,y) = \tilde{u}_i(x,y) - < \tilde{u}_i >_z (x,y)
\tag{25}
$$

where $<>_z$ denotes an average in the z direction only. The ensemble averaged root-mean-square (*rms*) values were subsequently obtained as

$$\tilde{u}_{rms}(x,y) = \sqrt{\frac{<\tilde{u}'(x,y)^2>}{N_{stat}}} \tag{26}$$

where $<>$ denotes an average in z and in time, and N_{stat} is the number of time steps used to compute the statistics. The rotating channel flow simulation began with a fully-developed channel flow solution obtained from previous research, and needed about 10,000 physical time steps to become statistically stationary under the influence of the system rotation. The turbulent statistics (e.g $\tilde{u}_{rms}$) were collected over the following 10,000 physical time steps.

Shear stress and heat flux distributions were also computed as part of the turbulence statistics. The computed shear stress contributions were

$$\tau_{res} = -<\rho\tilde{u}''\tilde{v}''> \tag{27}$$

$$\tau_{vis} = -<\frac{\mu}{Re}\frac{\partial\tilde{u}}{\partial y}> \tag{28}$$

$$\tau_{sgs} = -<\mu_t\frac{\partial\tilde{u}}{\partial y}> \tag{29}$$

where τ_{res} is the resolvable Reynolds shear stress, τ_{vis} is the viscous shear stress, and τ_{sgs} is the modeled SGS stress. Similarly, the computed heat flux contributions were

$$q_{res} = -<\rho\tilde{v}''\tilde{T}''> \tag{30}$$

$$q_{con} = -<\frac{\mu c_p}{RePr}\frac{\partial\tilde{T}}{\partial y}> \tag{31}$$

$$q_{sgs} = -<\frac{\mu_t c_v}{Pr_t}\frac{\partial\tilde{T}}{\partial y}> \tag{32}$$

where q_{res} is the resolvable turbulent heat flux, q_{con} is the heat conduction, and q_{sgs} is the modeled SGS heat flux.

3.3 Results and Discussion

3.3.1 Channel Flows without Ribs

The simulations were run with a domain size of $2\pi \times 2 \times \pi$ with a grid that had $48 \times 64 \times 48$ control volumes in the x, y and z directions, respectively. A grid study (Dailey [2]) has shown that for low heating simulations without rotation, this grid size provided accurate results compared to DNS and experimental data. The near wall region is well-resolved. For the high heating case, the y^+ (based on averaged friction velocity) at the first grid point near the wall is less than 0.5.

No-slip velocity and zero normal pressure gradient boundary conditions were enforced at the upper and lower walls. The isoflux thermal wall boundary conditions were used for both walls. The dimensionless wall heat flux ($q_w = \frac{q_w^*}{C_p \rho_{ref} U_{ref} T_{ref}}$) was kept at 2×10^{-4} for the low heating case, and kept at 2×10^{-3} and -2×10^{-3} for high heating and high cooling cases, respectively.

Calculations were performed for four different cases: no heat transfer, low heating, high heating, and high cooling. The Reynolds number $Re = U(2\delta)/\nu$ (based on the channel width, 2δ, and reference velocity, U) was 5600, and the rotation number $Ro_b = |\Omega|(2\delta)/U$ was 0.144. (Note that Rossby number is defined as $Ro = U/(2|\Omega|D_H)$, which is a quarter of the inverse of the rotation number Ro_b.)

The results from first the case were compared with the DNS results (grid $96 \times 97 \times 128$) of Piomelli and Liu [6] for the isothermal rotating channel flow with $Re_b = U_b(2\delta)/\nu = 5700$ and $Ro_b = 0.144$. Since it was found from previous LES simulations that the contribution of SGS model to turbulent flux is small, it is interesting to do a simulation (coarse grid DNS) without any model using the same grid resolution as that of LES ($48 \times 64 \times 48$).

Figure 1 shows the *rms* distributions (normalized by the average value of u_τ on two walls) for velocity fluctuations in x, y, and z directions, respectively. The *rms* fluctuations are enhanced near the unstable side (trailing, $y = 1.0$) but reduced near the stable side of the channel (leading, $y = -1.0$). It is noticeable that the profile of v_{rms} becomes a one-peak distribution instead of the two-peak distribution obtained without rotation. This is also due to the fact that the Coriolis force acts in the y direction. These results agree well with those of Piomelli[6]'s, validating the current LES formulation. The coarse grid DNS data, in general, slightly overestimate velocity fluctuations compared with the LES data. There is an overshoot for the coarse grid DNS in the prediction of

velocity fluctuations near the upper (top) wall. The reason might be that the current grid resolution $(48 \times 64 \times 48)$ is not fine enough for DNS. LES has better damping behavior at the near wall region with the aid of the SGS model.

Tables 1 (a) and (b) list some parameters at both walls.

where the friction velocity is

$$u_\tau = \sqrt{\frac{\tau_w}{\rho_w}} \tag{33}$$

$\Delta T = T_{w,top} - T_{w,bot}$ is the temperature change across the normal direction, and T_b is the bulk temperature.

$$T_b = \frac{\int_{-1}^{1} \rho u T \, dy}{\int_{-1}^{1} \rho u \, dy} \tag{34}$$

Table 1 (a)

Summary of the numerical calculations

Case	$u_{\tau,top}$	$u_{\tau,bot}$	$\frac{\Delta T}{T_b}$
Low Heating	0.0701	0.0470	-0.0585
High Heating	0.0889	0.0759	-0.594
High Cooling	0.0686	0.0263	$+0.471$

Table 1 (b)

Case	Nu_{top}	Nu_{bot}	$C_{f,top}$	$C_{f,bot}$
Low Heating	60.04	20.70	0.00551	0.00228
High Heating	66.29	18.47	0.00587	0.00279
High Cooling	62.14	18.57	0.00544	0.00212

The Nusselt numbers and the friction coefficient are defined as
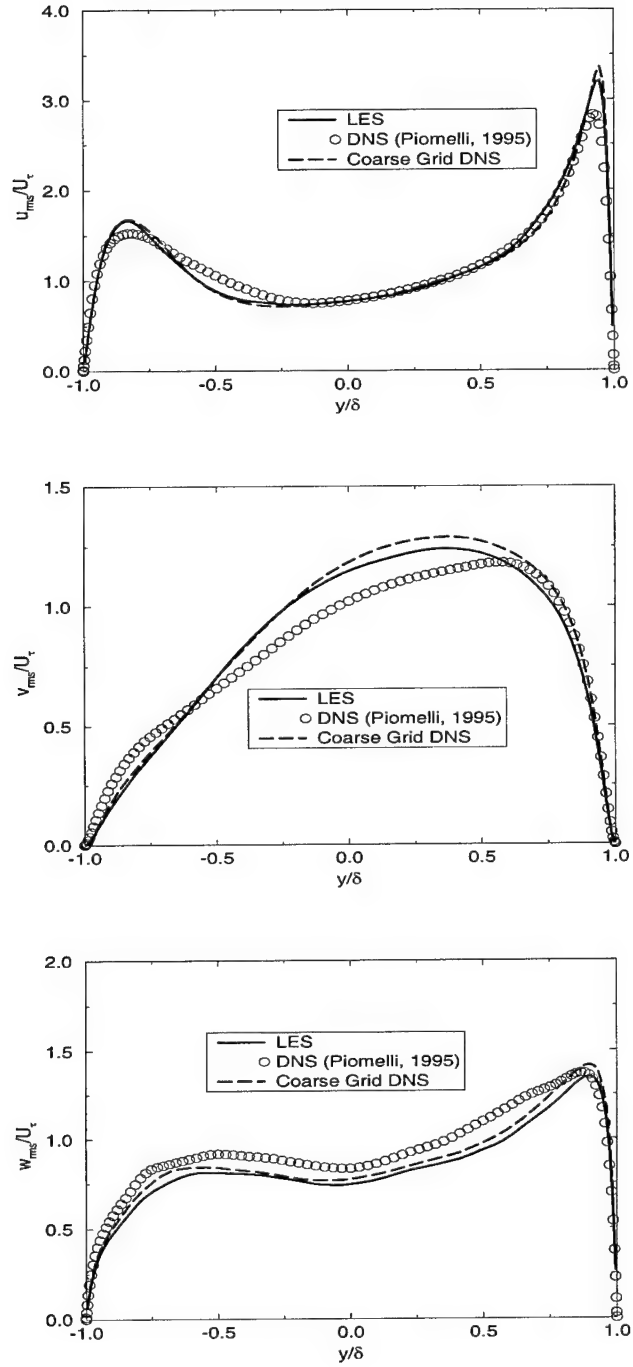
$$Nu = \frac{2h\delta}{k_b} \tag{35}$$

Figure 1: Streamwise, normal, and spanwise velocity *rms* distributions, isothermal case

$$C_f = \frac{\tau_w}{\frac{1}{2}\rho_b U_b^2} \tag{36}$$

where h is the heat transfer coefficient, k_b the bulk thermal conductivity, ρ_b and U_b are the bulk density and velocity, respectively.

The ratio of friction velocity at the top wall to that at the bottom wall is approximately 2.6, 1.5, and 1.2 for high cooling, low heating, and high heating, respectively. The high cooling case reacted most strongly to the system rotation as indicated by the significant difference between its two friction velocities. The low heating case has a relative temperature change ($\Delta T/T_b$) of 5.85%, but high heating and high cooling cases have much larger temperature change, namely, 59.4% and 47.1%, respectively. It is found that Nusselt number at the top wall (or the unstable side) is slightly more than three times as large as that at the bottom wall (or the stable side). Friction coefficients at the top wall are around two times larger than those at the bottom wall.

Figure 2 illustrates the streamwise velocity profiles for high heating (HH), high cooling (HC) and low heating (LH) cases in global and semi-local coordinate systems. The influence of rotation is reflected in the asymmetric distribution of velocities for all three cases. The U velocity profile for HC is above that of LH, but the profile for HH is below that of LH. This is, in part, because in the figures the streamwise velocity has been normalized by the average of u_τ at the two walls and u_τ is significantly influenced by property variations in the flow.

Huang et al. [20] have proposed a semi-local definition of friction velocity, in which the local density is used instead of the wall density.

$$u_\tau^* = \sqrt{\frac{\tau_w}{\rho}}$$

When u_τ^* is used to replace u_τ, the resulting semi-local distribution shows that the three profiles collapsed toward the low heating curve.

The mean temperature profiles are plotted in global coordinates and semi-local coordinates in Fig. 3. The T_τ and T_τ^* are defined as below,

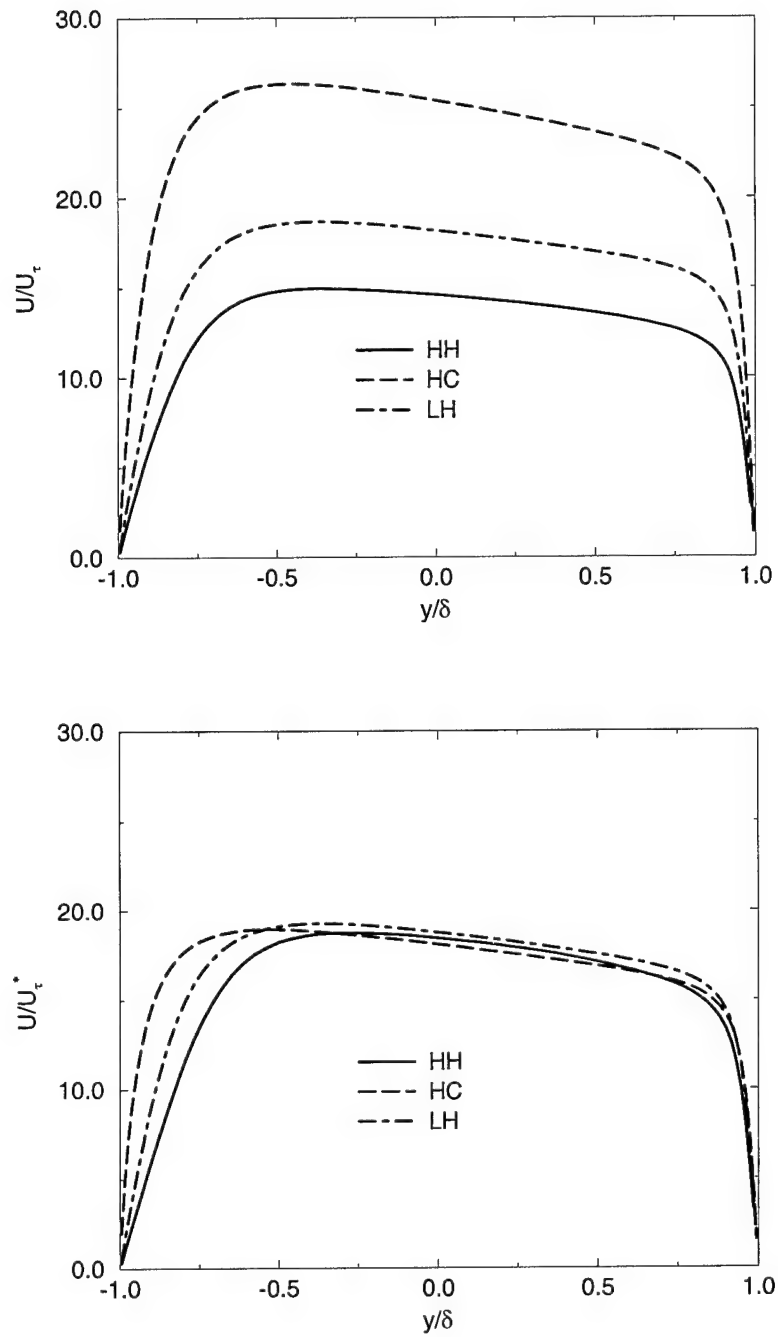$$T_\tau = \frac{q_w}{\rho_w c_p u_\tau}; \; T_\tau^* = \frac{q_w}{\rho(y) c_p u_\tau^*} \tag{37}$$

15

Figure 2: Profiles of u velocity in global and semi-local coordinates

As for the velocity profiles, the high heating and high cooling temperature profiles in global coordinates departed from the low heating results. However, the spread in the curves is greatly decreased when semi-local coordinates are used. Again, non-symmetry has been observed in those averaged temperature distributions.

The root-mean-squares of the velocity fluctuations with respect to Reynolds ensemble averages are plotted in global coordinates in Fig. 4. Again, larger velocity fluctuations were found near the unstable side as a consequence of rotation, and the high heating and cooling values varied significantly from the low heating result. Again, the values are normalized by the average of u_τ for the two walls.

Figure 5 shows the viscous, resolved, and modeled SGS shear stress distributions normalized by the average of the two wall shear stresses. The results indicate that rotation increased the shear stress near the unstable side but suppressed the shear stress near the stable side.

Figure 6 shows the heat conduction, resolved turbulent heat flux and modeled SGS heat flux distribution normalized by the wall heat flux. The same trends were observed as for the shear stress distributions, suggesting that heat transfer was increased near the unstable side but decreased near the stable side because of rotation.

3.3.2   Channel Flows with Ribs

The geometry and coordinate systems for the ribbed channel cases are depicted in Fig. 7. The ribs were directly opposed and aligned normal to the main flow direction. The ratio of rib spacing to rib height was 10 and rib height to channel height was 0.1. Calculations were performed for three different cases with a $(72 \times 62 \times 72)$ grid size:no rotation, medium rotation, and high rotation. Uniform heat flux was applied to the channel to investigate the effects of property variations with temperature. The Reynolds number was 5600. The detailed information is given in Table 2.
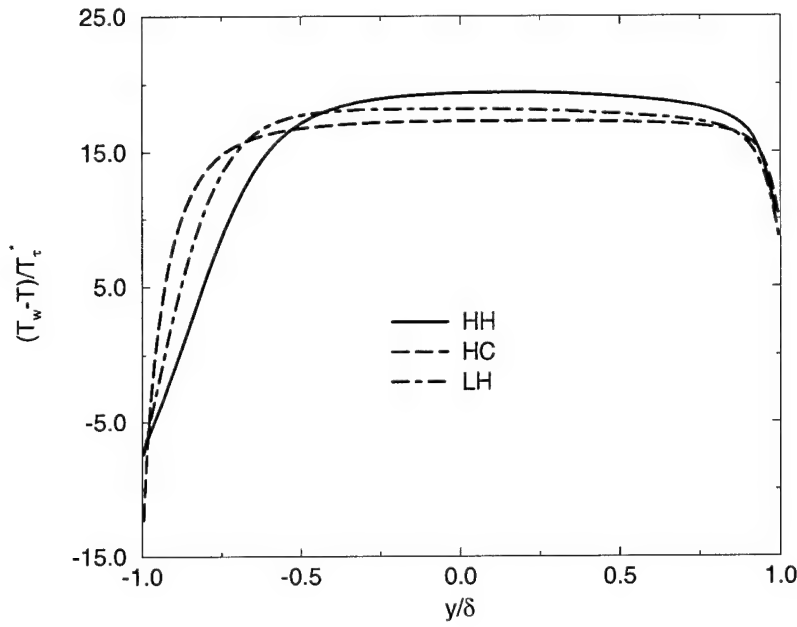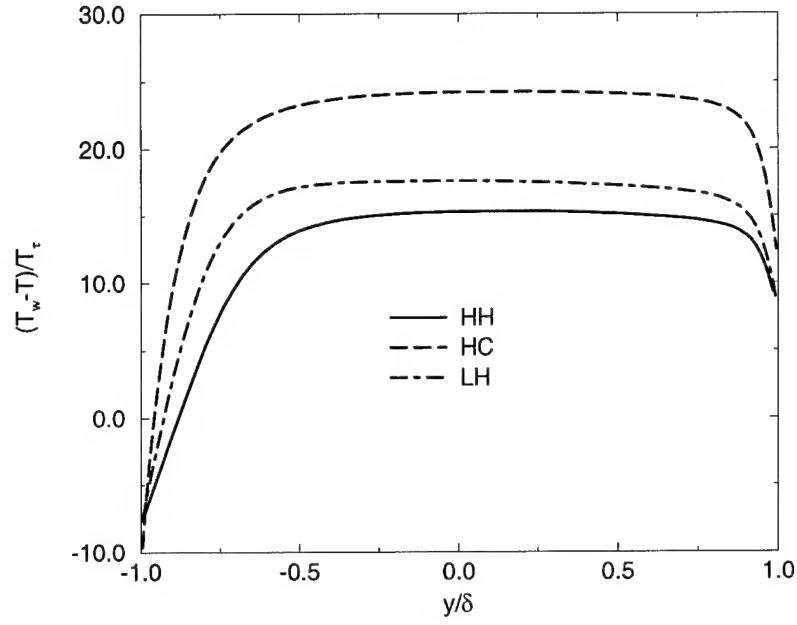
17

Figure 3: Profiles of temperature in global and semi-local coordinates; T_w is the average of the two wall temperatures
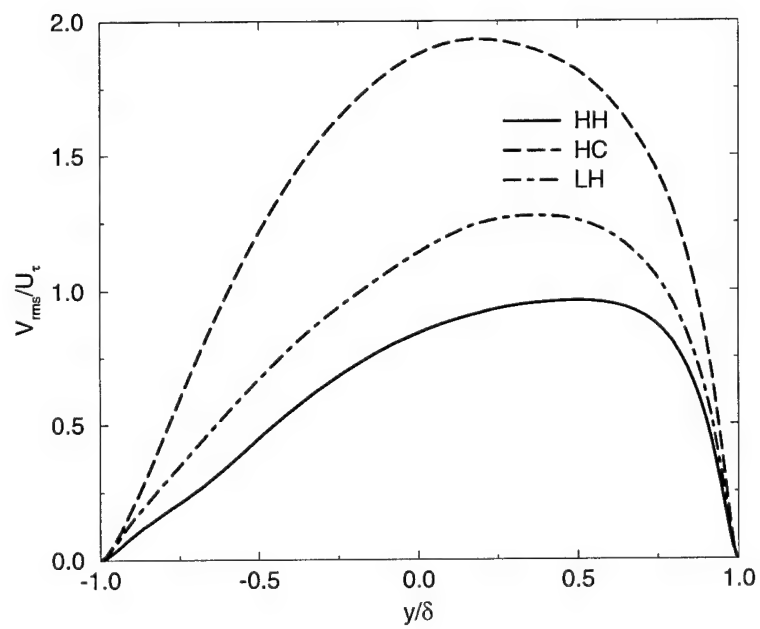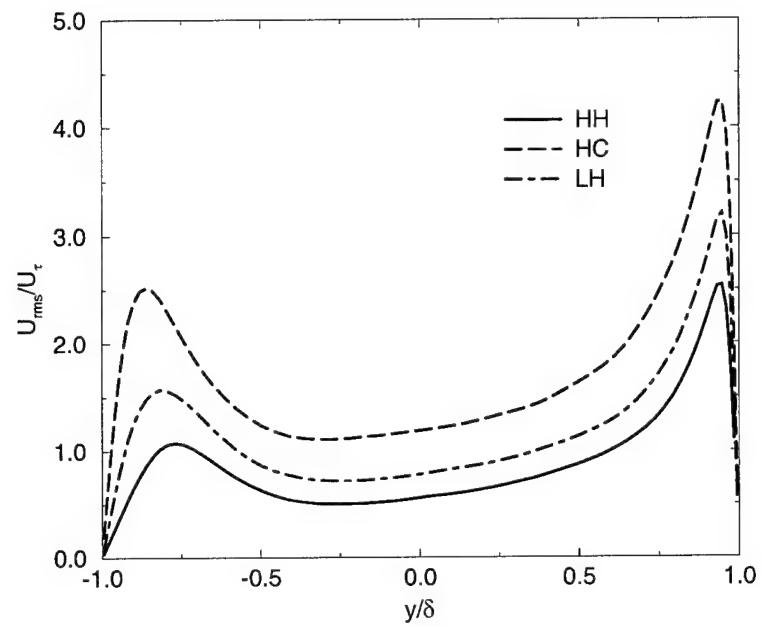
Figure 4: Velocity *rms* in x and y
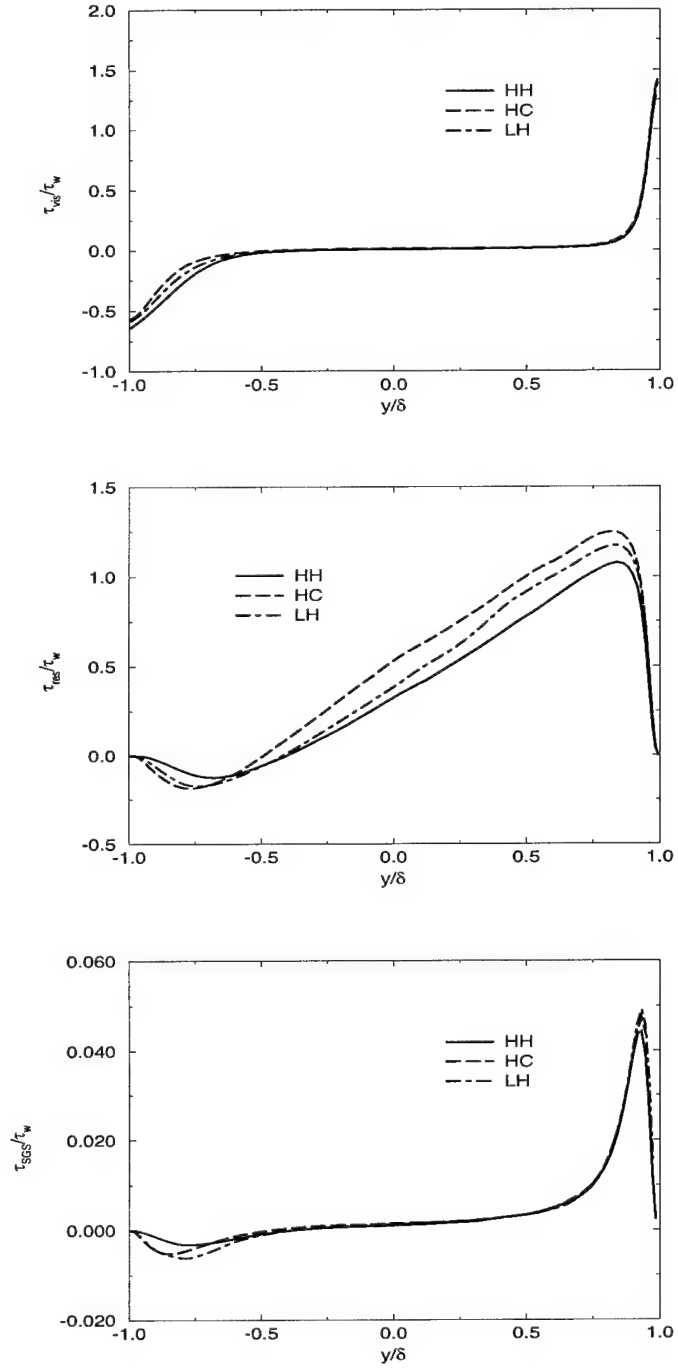
Figure 5: Viscous, Resolved, and SGS stresses
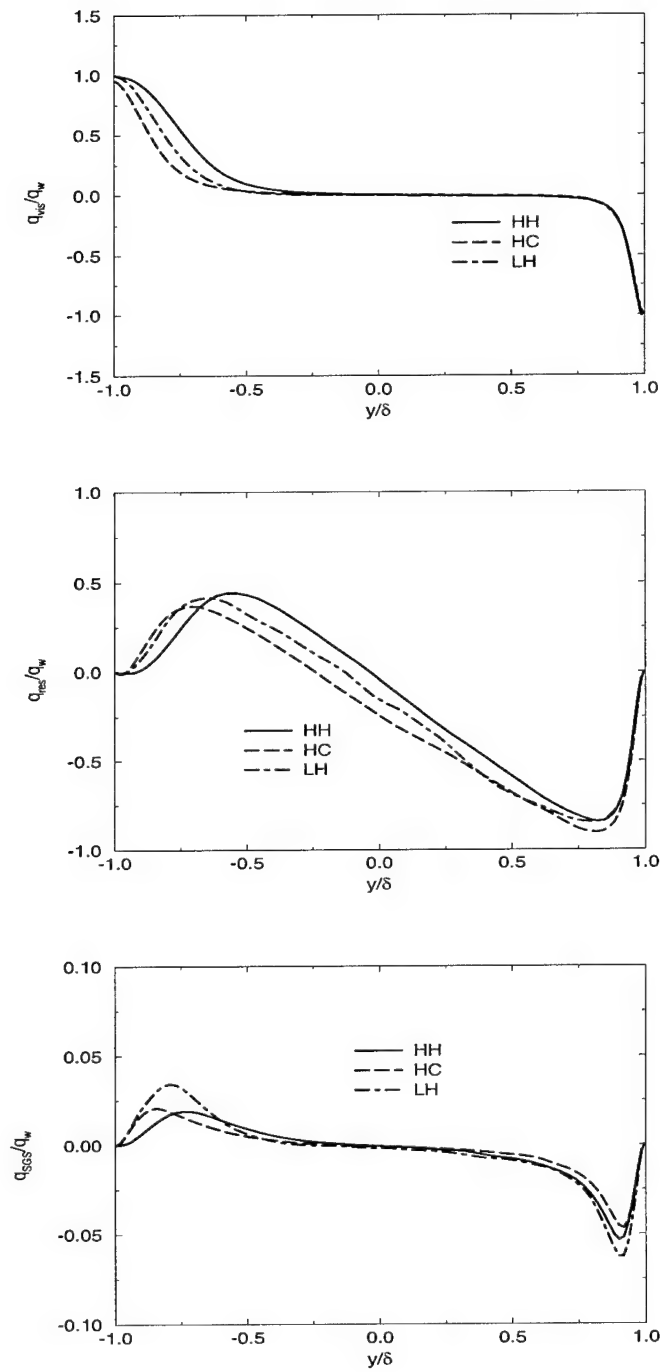
Figure 6: Viscous, Resolved, and SGS heat fluxes
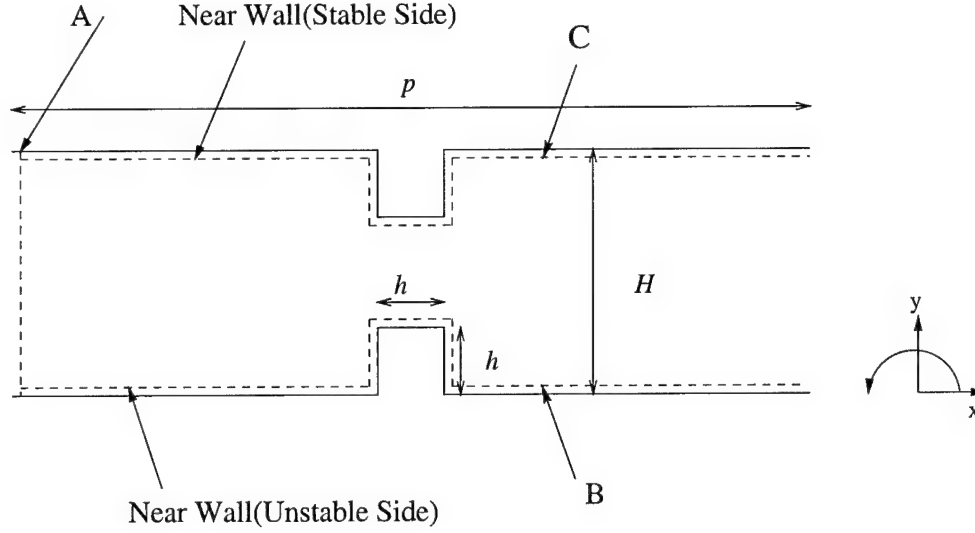
Figure 7: Schematic of the computational domain for the ribbed channel

Table 2

Parameters for three rotational cases

CASE	Ro_b	q_w
I	0.00 (No Rotation)	2×10^{-3}
II	0.15 (Medium Rotation)	2×10^{-3}
III	0.30 (High Rotation)	2×10^{-3}

Figure 8 shows the corresponding *rms* distributions for turbulent intensities in the x, y, and z directions at section A. As we observed earlier, the Coriolis force tends to reduce and enhance the turbulent intensities near the stable side, and unstable side, respectively.

The friction coefficient (C_f) and the Nusselt number (Nu) along the wall at sections B and C are shown in Fig. 9. Since the profile is symmetric, only one distribution of C_f is shown for Case I. The reattachment length varied with different rotation numbers. Increasing rotation led to a decrease (or increase) in the reattachment length on the unstable (stable) side because the Coriolis force increases (decreases) turbulent mixing near the unstable (stable) side. The enhanced mixing on the unstable side resulted in higher levels of Nusselt number as can be seen in Fig. 9.
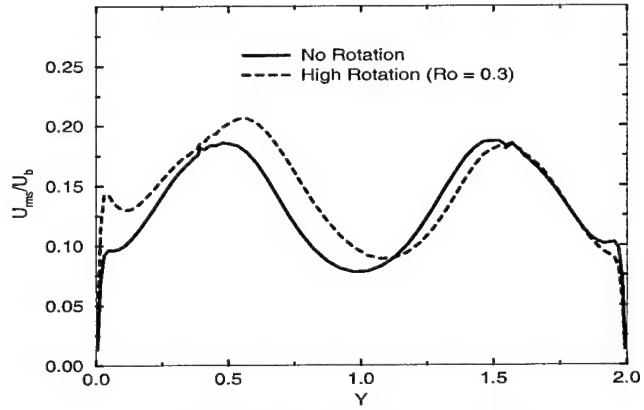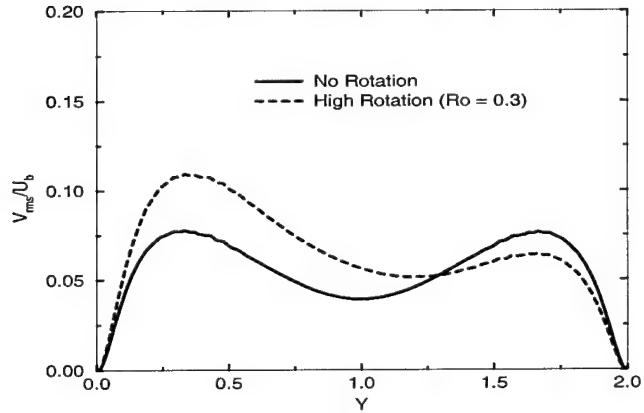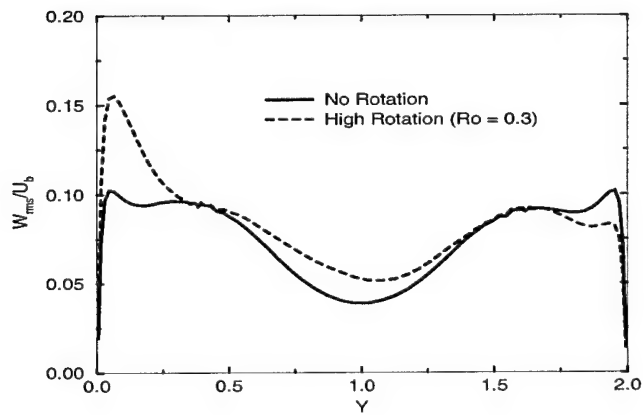
Figure 8: *Urms*, *Vrms*, and *Wrms* profiles at section A.

Overall, the Nusselt number increases rapidly and reaches a local maximum near the upstream corner of the rib where high levels of turbulent intensities are observed. Then, the Nusselt number decreases near the top of the rib. The Nusselt number keeps decreasing along the rear face of the rib due to the recirculation and increases to the second local maximum near reattachment. The heat transfer on the top of the rib increases about 35 % compared to stationary (non-rotating) case near the unstable side, but decreases about 20 % near the stable side. Similar order of magnitude differences compared to the stationary case are noticed in the downstream region. The flow pattern of streamlines for Case I (no rotation) and Case III (high rotation) are shown in Fig. 10. The separation bubbles on the front and rear faces of the ribs are clearly visible. Due to the large increasing pressure gradient on the top of the ribs, a small separation is induced (see Fig. 9). Behind the ribs, a rapid rise of the static pressure causes a larger separation region. For Case I, the reattachment length of the separation region is about 5h (5 × rib height) for both walls, but it is about 3h near the unstable side and 5.5h near the stable side for Case III.

3.4 Concluding Comments–Rotating Channels

The LES results (mean velocity and velocity fluctuations) agree well with Piomelli [6]'s DNS data for the incompressible isothermal rotating channel flow at a rotation number of 0.144.

Turbulent channel flow with low heating was calculated. Additionally, turbulent channel flows with constant wall heating or cooling rates of magnitudes large enough to cause significant variation in the temperature-dependent fluid properties were simulated. All those simulations were performed under the influence of spanwise system rotation.

In general, the system rotation was found to suppress turbulent velocity fluctuations and shear stress near the stable side of the channel, but enhance those fluctuations and shear stress near the unstable side. Accordingly, turbulent temperature fluctuations and turbulent heat flux are decreased near the stable side of the channel, but increased near the unstable side of the channel. The streamwise and spanwise *rms* velocity fluctuations can be seen to differ by about a factor of two near the two walls. The ratio of wall shear stress and heat flux on the two sides ranged between a factor of 2 and 3. The ratio of Nusselt numbers at the two walls was very nearly a factor of 3 as can be seen from Table 1(b).

The coarse grid DNS gave nearly as good results as LES, except that it overestimated the veloc-

Friction Factor

Nusselt Number
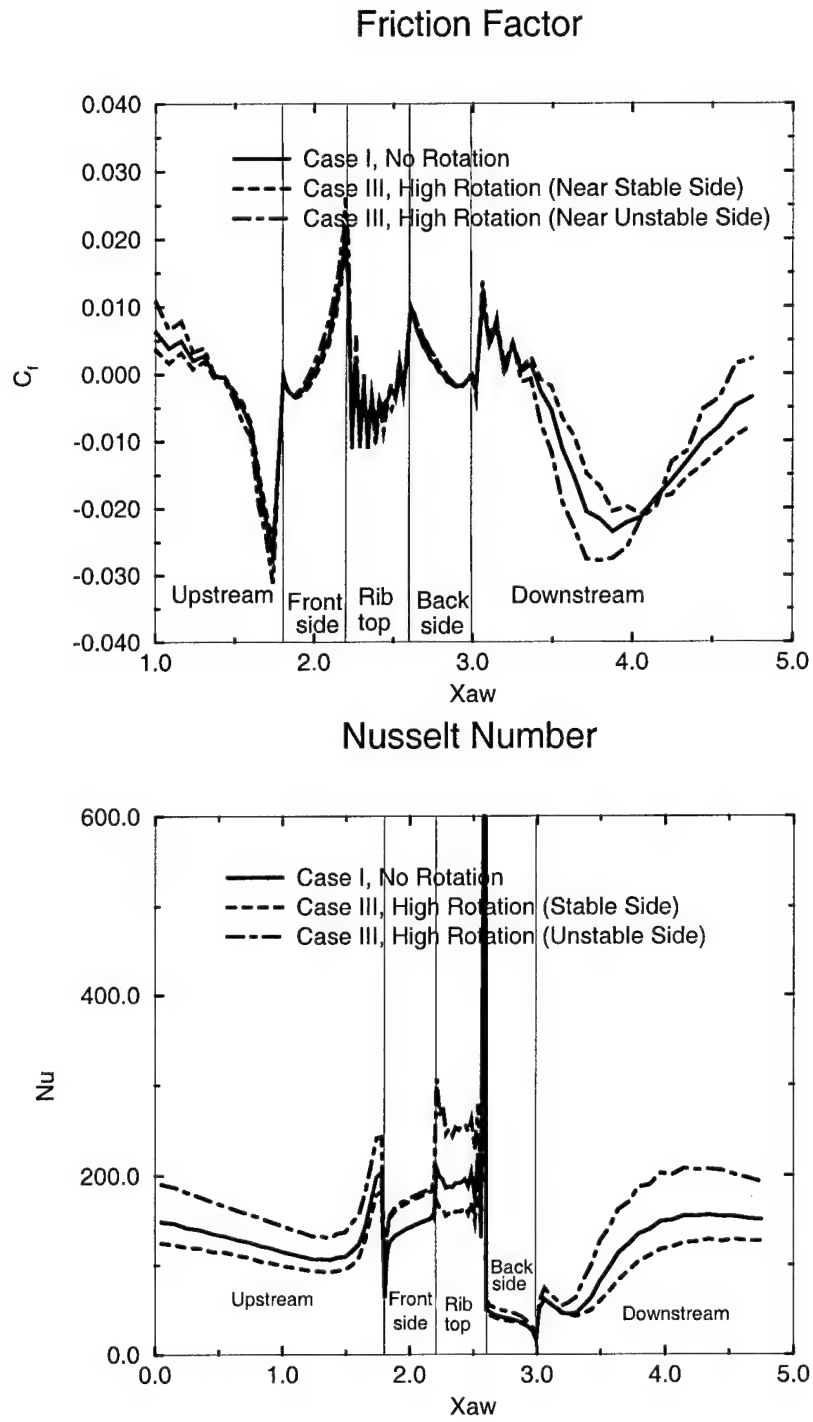
Figure 9: C_f and Nu profiles at section B and C (see Fig. 7 for section B and C)

25

Case I, No Rotation

Case III, High Rotation
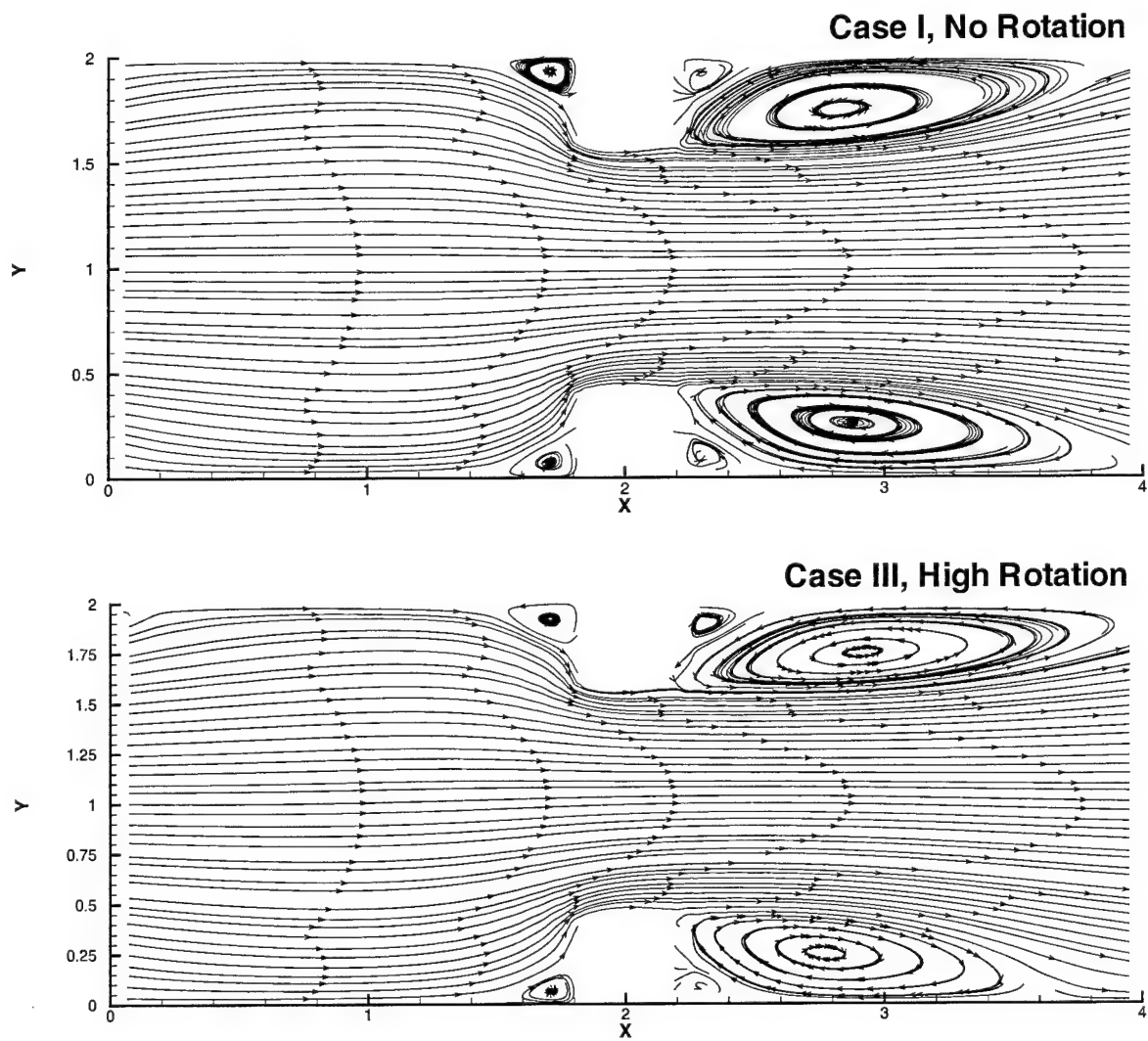
Figure 10: Streamlines for Cases I and III

26

ity fluctuations near the wall due to its lack of a dissipation mechanism. In addition, using semi-local coordinates instead of wall coordinates tends to collapse curves of high heating and low heating into that of low heating. It is interesting, too, that the distribution of *rms* of V velocity is changed significantly (from a two-peak profile to a one-peak profile) due to the Coriolis force acting in the y direction.

An investigation was also conducted on the effects of rotation on the heat transfer in a ribbed channel flow using large eddy simulation. Very consistent results were obtained indicating that rotation stabilizes the leading side and unstabilizes the trailing side. Urms, Vrms, Wrms, and friction factor, all consistently show that the turbulence structure is greatly altered by the rotation. The turbulence intensity is significantly higher near the unstable side. The reattachment length also shows sensitivity to rotation. The reattachment length on the stable side is increased due to the laminarization, while it is decreased on the unstable side. Rotation also influences the heat transfer in the flow. With rotation, the heat transfer was greatly enhanced on the unstable side and reduced on the stable side. It is found that the temperature profile is no longer symmetric due to the Coriolis force.

4 Large Eddy Simulation of Turbulent Heat Transfer in a Square Duct with and without Rotation

4.1 Introduction

Turbulent flow inside a rotating square duct has many engineering applications including turbine blade cooling. In turbulent duct flows, Prandtl's secondary flow of the second kind has a significant effect on the transport of heat and momentum. This secondary flow causes distortion of the isolines of mean velocity, temperature, and their fluctuations. Heating changes the structures of the near wall turbulence which in turn changes the mean and fluctuation values as well as Reynolds stress components. Different heating arrangements have different effects. With rotation, Coriolis and centrifugal buoyancy forces cause a more complicated secondary flow pattern and, as a consequence, modify heat transfer coefficients. The objective of this portion of the study is to expand the capability of the current LES code to correctly predict complex turbulent flow phenomena and to gain a better understanding of the physics of turbulent flow in rotating passages. In the following sections, we will present the numerical approach first and then the results of various cases.

4.2 Approach

The numerical formulation used in the research is based on a finite volume discretization of the Favre-filtered compressible Navier-Stokes equations. A finite volume LU decomposition scheme coupled with time derivative preconditioning is used to simulate compressible three-dimensional turbulent flows at low Mach numbers. The whole calculation domain is divided into two parts (see Fig. 11). Spatially periodic boundary conditions are applied to the first (or, the inflow generator) part of the domain, and the fully developed exit velocity profile of this part is used as the entrance profile of the second (or, the test section) part. The pressure at the same entrance is interpolated from the interior domain, however. To ensure the mass flow rates of the two parts the same, the temperature at the entrance of the test section is recalculated according to the interpolated pressure so that the density is unchanged across the entrance section. Characteristic out-flow conditions are applied to the second part. This allows the flow to develop further as it responds to the heating condition.
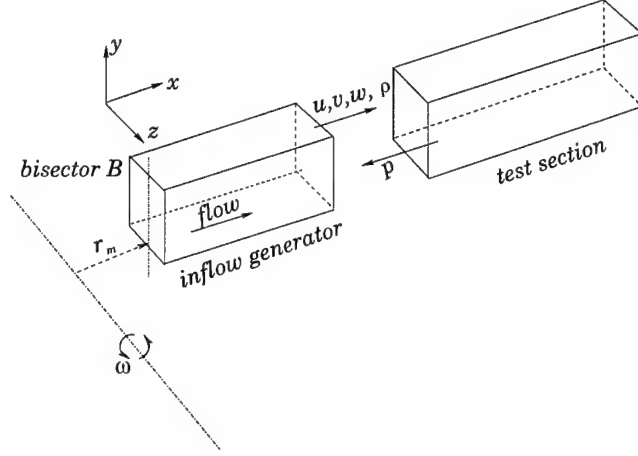
Figure 11: Sketch of the computational domain

4.2.1 LU Decomposition Method

The filtered nondimensional compressible Navier-Stokes equations can be recast in vector form as

$$\frac{\partial \bar{\mathbf{U}}}{\partial t} + \frac{\partial \bar{\mathbf{F}}_i}{\partial x_i} = \bar{\mathbf{S}},\tag{38}$$

where

$$\bar{\mathbf{U}} = (\bar{\rho}, \bar{\rho}\tilde{u}, \bar{\rho}\tilde{v}, \bar{\rho}\tilde{w}, \bar{\rho}\tilde{e})^T.\tag{39}$$

The resolved fluxes $\bar{\mathbf{F}}_i$ are

$$\bar{\mathbf{F}}_i = \begin{pmatrix} \bar{\rho}\tilde{u}_i \\ \bar{\rho}\tilde{u}_i\tilde{u}_1 - \hat{\sigma}_{i1} + \tau_{i1} \\ \bar{\rho}\tilde{u}_i\tilde{u}_2 - \hat{\sigma}_{i2} + \tau_{i2} \\ \bar{\rho}\tilde{u}_i\tilde{u}_3 - \hat{\sigma}_{i3} + \tau_{i3} \\ \bar{\rho}\hat{e}\tilde{u}_i - \tilde{u}_j\hat{\sigma}_{ij} + \hat{q}_i + q_{ti} \end{pmatrix},\tag{40}$$

where

$$\hat{\sigma}_{ij} = -\bar{p}\delta_{ij} + \frac{2\bar{\mu}}{Re_r}(\bar{S}_{ij} - \frac{1}{3}\bar{S}_{kk}\delta_{ij}),\tag{41}$$

$$\tau_{ij} = \bar{\rho}(\widetilde{u_iu_j} - \tilde{u}_i\tilde{u}_j),\tag{42}$$

$$\hat{e} = c_v\tilde{T} + \frac{1}{2}\tilde{u}_i\tilde{u}_i,\tag{43}$$

$$\hat{q}_i = -\frac{c_p\bar{\mu}}{Re_rPr}\frac{\partial \tilde{T}}{\partial x_i}\tag{44}$$

29

and

$$q_{ti} = \bar{\rho} c_v (\widetilde{Tu_i} - \tilde{T}\tilde{u}_i). \tag{45}$$

The source term $\bar{\mathbf{S}}$ includes possible body forces. In the above equations, the subgrid-scale stress and heat flux tensors τ_{ij}, q_{ti} are modeled with the localized dynamic SGS model of Piomelli and Liu [6]. Coupled with the equation of state $p = \bar{\rho}R\bar{T}$, the above system can be solved by a *LU* decomposition method. For the sake of notational simplicity, in the following text the overbar for the grid scale variables will be dropped. Equation (38) can be recast in terms of primitive variables as

$$[T]\frac{\partial \mathbf{W}}{\partial t} + \frac{\partial \mathbf{F}_i}{\partial x_i} = \mathbf{S}, \tag{46}$$

where

$$\mathbf{W} = (p, u, v, w, T)^T, \tag{47}$$

and $[T]$ is Jacobian matrix:

$$[T] = \frac{\partial \mathbf{U}}{\partial \mathbf{W}}. \tag{48}$$

Eq. (46) can be integrated throughout the control volume Ω and becomes

$$\int_\Omega [T]\frac{\partial \mathbf{W}}{\partial t} d\Omega + \int_\Omega \frac{\partial \mathbf{F}_i}{\partial x_i} d\Omega = \int_\Omega \mathbf{S} d\Omega. \tag{49}$$

Using the Gauss divergence theorem, the above equation becomes

$$\int_\Omega [T]\frac{\partial \mathbf{W}}{\partial t} d\Omega + \oint_{\partial\Omega} \mathbf{F}_i \vec{e}_i \cdot d\vec{S} = \int_\Omega \mathbf{S} d\Omega, \tag{50}$$

where $\partial\Omega$ is the surface surrounding the control volume Ω and $\vec{e}_i$ is the unit vector in x_i direction. When Cartesian hexahedral control volumes are used, the above equation can be approximated in every control volume as

$$[T]\frac{\partial \mathbf{W}}{\partial t}\Omega + \sum_{j=1}^{6} \mathbf{F}_{ij} n_{ji} S_j = \mathbf{S}\Omega, \tag{51}$$

where summation convention does not hold for index j. $\mathbf{F}_{ij}$ is the value of $\mathbf{F}_i$ evaluated at surface j; n_{ji} is the projection of the unit outward normal $\vec{n}_j$ of surface $\vec{S}_j$ in the x_i direction. Time derivative preconditioning developed by Pletcher and Chen [3] is adopted to overcome the singularity

30

caused by low Mach number. This preconditioning introduces a pseudo temporal derivative into the equation:

$$[\Gamma]\frac{\partial \mathbf{W}}{\partial \tau}\Omega + [T]\frac{\partial \mathbf{W}}{\partial t}\Omega + \sum_{j=1}^{6}\mathbf{F}_{ij}n_{ji}S_j = \mathbf{S}\Omega, \tag{52}$$

where $[\Gamma]$ is the preconditioning matrix and τ is the pseudo temporal variable. This pseudo temporal derivative term is discretized as

$$\frac{\partial \mathbf{W}}{\partial \tau} \sim \frac{\Delta \mathbf{W}}{\Delta \tau}, \tag{53}$$

where

$$\Delta \mathbf{W} = \mathbf{W}^{(m+1)} - \mathbf{W}^{(m)}. \tag{54}$$

and m denotes the pseudo time step. The physical temporal derivative is evaluated with a second order, 3-point finite difference scheme

$$\frac{\partial \mathbf{W}}{\partial t} \sim \frac{3\mathbf{W}^{(m+1)} - 2\mathbf{W}^{(n)} + \mathbf{W}^{(n-1)}}{2\Delta t}, \tag{55}$$

or in the "Δ form" as

$$\frac{\partial \mathbf{W}}{\partial t} \sim \frac{3\Delta \mathbf{W}}{2\Delta t} + \frac{3\mathbf{W}^{(m)} - 2\mathbf{W}^{(n)} + \mathbf{W}^{(n-1)}}{2\Delta t}, \tag{56}$$

where n denotes the physical time step. The flux term $\mathbf{F}_i$ is decomposed into two parts: the inviscid part $\mathscr{F}_i$ and another part $\mathbb{F}_i$, which takes care of the viscous and subgrid-scale terms. $\mathscr{F}_i$ is treated implicitly while $\mathbb{F}_i$ is treated explicitly. $\mathscr{F}_i$ at pseudo time step $m+1$ is approximated as

$$\mathscr{F}_i^{(m+1)} \approx \mathscr{F}_i^{(m)} + [A]_i\Delta \mathbf{W}, \tag{57}$$

where

$$[A]_i = \frac{\partial \mathscr{F}_i}{\partial \mathbf{W}}. \tag{58}$$

Thus

$$\mathbf{F}_{ij}^{(m+1)} \approx \mathscr{F}_{ij}^{(m)} + ([A]_i\Delta \mathbf{W})_j + \mathbb{F}_{ij}^{(m)} = \mathbf{F}_{ij}^{(m)} + ([A]_i\Delta \mathbf{W})_j, \tag{59}$$

in which $\mathbf{F}_{ij}^{(m)}$ is evaluated with $\mathbf{W}^{(m)}$ at face j (which can be obtained by averaging $\mathbf{W}^{(m)}$ of two neighboring control volumes); while $([A]_i \Delta \mathbf{W})_j$ can be split into

$$([A]_i \Delta \mathbf{W})_j \approx ([A]_i^+ \Delta \mathbf{W})_{J-1} + ([A]_i^- \Delta \mathbf{W})_{J+1}, \tag{60}$$

where $J-1$ and $J+1$ denote two neighboring control volumes separated by face j and

$$[A]_i^\pm = \frac{1}{2}[A]_i \pm max|\lambda_{[A]_i}|[I], \tag{61}$$

in which $\lambda_{[A]_i}$ are the eigenvalues of $[A]_i$. Then every term in Eq. (52) is expressed with $\mathbf{W}^{(m)}$ and $\Delta \mathbf{W}$ and the equation can be rewritten as

$$([L] + [D] + [U]) \Delta \mathbf{W} = -\mathscr{R}. \tag{62}$$

Then the preconditioned time accurate governing equation is solved by the lower-upper symmetric Gauss-Seidel (LU-SGS) scheme [24].

4.2.2 Outflow Boundary Treatment

At the outlet of the test section, Navier-Stokes characteristic boundary conditions are applied. This method, which intends to provide time-accurate boundary conditions, was proposed by Thompson [25, 26] and then was further developed by Poinsot & Lele [27].

Consider the characteristic form of Eq. (46) in x_1 direction (since the normal of the outlet is in x_1 direction in present work):

$$[T]\frac{\partial \mathbf{W}}{\partial t} + \frac{\partial \mathscr{F}_1}{\partial x_1} + \mathbb{C} = \mathbf{0}, \tag{63}$$

or

$$[T]\frac{\partial \mathbf{W}}{\partial t} + [A]_1\frac{\partial \mathbf{W}}{\partial x_1} + \mathbb{C} = \mathbf{0}, \tag{64}$$

where the source term is neglected and $\mathbb{C}$ are flux derivative terms excluding $\frac{\partial \mathscr{F}_1}{\partial x_1}$. Let $[\mathscr{A}] = [T]^{-1}[A]_1$, then the above equation becomes

$$\frac{\partial \mathbf{W}}{\partial t} + [\mathscr{A}]\frac{\partial \mathbf{W}}{\partial x_1} + [T]^{-1}\mathbb{C} = \mathbf{0}. \tag{65}$$

32

Let

$$[\Lambda] = [S]^{-1}[\mathscr{A}][S],\tag{66}$$

where $[\Lambda]$ is the diagonal matrix whose elements are eigenvalues of $[\mathscr{A}]$, and the rows of $[S]^{-1}$ are left eigenvectors. For an ideal gas,

$$[\Lambda] = \begin{pmatrix} u_1 + c \\ u_1 - c \\ u_1 \\ u_1 \\ u_1 \end{pmatrix},\tag{67}$$

where c is the local sound speed and

$$c = \sqrt{\frac{\gamma p}{\rho}},\tag{68}$$

where γ is the specific heat ratio. Then, after multiplying $[S]^{-1}$, Eq. (65) becomes

$$[S]^{-1}\frac{\partial \mathbf{W}}{\partial t} + \overbrace{[\Lambda][S]^{-1}\frac{\partial \mathbf{W}}{\partial x_1}}^{[\Pi]} + [S]^{-1}[T]^{-1}\mathbb{C} = \mathbf{0}.\tag{69}$$

where the underbrace under $[\Lambda][S]^{-1}\frac{\partial \mathbf{W}}{\partial x_1}$ is labeled $\mathscr{L}$.

By employing the characteristic form, waves with different velocities can be determined separately. At the boundary, waves leaving the domain are calculated using interior points and one-sided differences. Waves propagating into the domain, however, should be estimated by available information outside the domain and also by examination of the above equation. In the current situation, $\mathscr{L}_2$ is the only incoming wave since its speed is negative ($u_1 - c$). By multiplying $[S]$, Eq. (69) becomes

$$\frac{\partial \mathbf{W}}{\partial t} + [S]\mathscr{L} + [T]^{-1}\mathbb{C} = \mathbf{0}.\tag{70}$$

A constant pressure at infinity is used as the outlet boundary condition in the present work. This is a partially-reflecting condition. From Eq. (70), by neglecting the transverse and viscous terms, which is also called the local one-dimensional inviscid (LODI) assumption, we have

$$\frac{\partial p}{\partial t} + \frac{\gamma}{\gamma - 1}\rho(\mathscr{L}_1 + \mathscr{L}_2) = 0.\tag{71}$$

33

Let

$$\frac{\partial p}{\partial t} = 0,$$ (72)

then

$$\mathcal{L}_2 = -\mathcal{L}_1.$$ (73)

Since $\mathcal{L} = [\Pi]\frac{\partial \mathbf{W}}{\partial x_1}$, the matrix $[\Pi]$ is changed into $[\Pi]'$ according to Eq. (73). To take account of the effect of pressure at infinity, Eq. (73) is modified [27] as

$$\mathcal{L}_2 = -\mathcal{L}_1 + K(p - p_\infty),$$ (74)

where K is a positive constant and can be determined by

$$K = \frac{\sigma(1 - \mathcal{M}^2)c}{L},$$ (75)

in which σ is equal to 0.27 [28], $\mathcal{M}$ is the maximum Mach number in the flow, L is a characteristic size of the domain. The waves at the outlet boundary thus becomes

$$\mathcal{L} = [\Pi]'\frac{\partial \mathbf{W}}{\partial x_1} + \mathbf{b},$$ (76)

where

$$\mathbf{b} = \left\{ \begin{array}{c} 0 \\ K(p - p_\infty) \\ 0 \\ 0 \\ 0 \end{array} \right\}.$$ (77)

And Eq. (69) becomes

$$[S]^{-1}\frac{\partial \mathbf{W}}{\partial t} + [\Pi]'\frac{\partial \mathbf{W}}{\partial x_1} + \mathbf{b} + [S]^{-1}[T]^{-1}\mathbb{C} = \mathbf{0}.$$ (78)

34

Multiplying by $[T][S]$, Eq. (78) becomes

$$[T]\frac{\partial \mathbf{W}}{\partial t} + [A]'_1 \frac{\partial \mathbf{W}}{\partial x_1} + \mathbb{C}' = \mathbf{0}, \tag{79}$$

or

$$[T]\frac{\partial \mathbf{W}}{\partial t} + \frac{\partial \mathscr{F}'_1}{\partial x_1} + \mathbb{C}' = \mathbf{0}, \tag{80}$$

where

$$[A]'_1 = [T][S][\Pi]'$$
$$\mathbb{C}' = \mathbb{C} + [T][S]\mathbf{b}. \tag{81}$$

Equation (80) is of the same form of Eq. (63) and should be applied at the outlet surface as Fig. 12 indicates. At the outlet control volume ni, the x_1 direction flux derivative term in Eq. (52) should
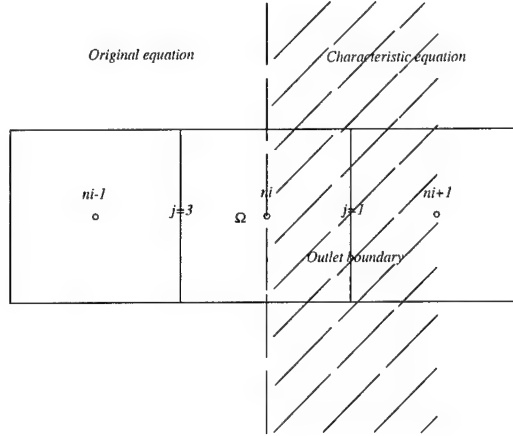

Figure 12: Sketch of the outlet boundary

be evaluated according to Eq. (63) at face $j = 3$ (interior face) and according to Eq. (80) at face $j = 1$ (outlet boundary face), respectively. Note that $\mathscr{F}'_1$ is unknown (though we do know $\frac{\partial \mathscr{F}'_1}{\partial x_1}$ and $\frac{\partial \mathscr{F}'_1}{\partial \mathbf{W}}$, which is $[A]'_1$), thus we evaluate the integral of the x_1 direction flux derivative term through the

Table 1: Computational details, cases without rotation

Case	Re_b	Grid Size	q_w	T_w/T_b
1	8100	$180 \times 40 \times 40$	0.0	1.0
2	16200	$180 \times 40 \times 40$	0.0	1.0
3	8100	$180 \times 40 \times 40$	-	1.23
4	8100	$180 \times 40 \times 40$	2.0×10^{-3}	-
5	8100	$180 \times 40 \times 40$	-	2.0
6	16200	$180 \times 40 \times 40$	-	1.23

boundary control volume ni as

$$
\begin{aligned}
\int_\Omega \frac{\partial \mathbf{F}_1}{\partial x_1} d\Omega \approx\; & (\mathbf{F}_{1ni}^{(m)} - \mathbf{F}_{13}^{(m)}) S_{13} \\
& + \; [([A]_1 \Delta \mathbf{W})_{ni} - ([A]_1 \Delta \mathbf{W})_3] S_{13} \\
& + \; \frac{\partial \mathscr{F}_1'^{\,(m)}}{\partial x_1} \frac{\Omega}{2} \\
& + \; [([A]_1' \Delta \mathbf{W})_1 - ([A]_1' \Delta \mathbf{W})_{ni}] S_{13},
\end{aligned}
\tag{82}
$$

where S_{13} is the area of face $j = 1$ and $j = 3$. The subscript ni means the value at the center of control volume ni. Then the outflow boundary control volume can also be expressed in the form of Eq. (62) and be solved by the LU-SGS scheme.

4.3   Results and Discussion

4.3.1   Turbulent Heat Transfer in a Square Duct Without Rotation

The Isothermal Duct

To validate our code, an isothermal duct case was simulated. The computational details are in Table 1. The results are compared with DNS results [29] and experimental data [30, 31]. The mean quantities are obtained by ensemble averaging throughout the test section in the x direction and in time. Figure 13 shows the streamwise mean velocity along the wall bisector. The root mean square (*r.m.s.*) values of u, v and w along the wall bisector are presented in Fig. 14. Both mean velocity and velocity fluctuations are normalized by the friction velocity averaged over four walls. If the mean velocity is normalized by the local friction velocity, the profile will move closer to the Nikuradse equation ('log-law'). The friction velocity and distance in wall units (dimensional) are
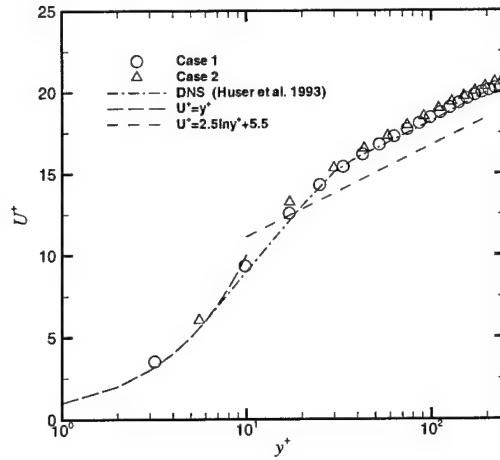
36

Figure 13: Streamwise mean velocity

defined as

$$u_\tau = \sqrt{\frac{\tau_w}{\rho_w}}$$
$$y^+ = \frac{\delta_y u_\tau}{v_w},$$

(83)

where τ_w is the wall shear stress and δ_y is the distance to the wall. Figure 15 shows the local wall shear stress normalized by the averaged wall shear stress along one wall compared with the DNS results [29]. Figure 16 shows a comparison between the measurements of U/U_c and W/U_c at different locations [30] with simulation results where U_c is the streamwise mean velocity at the center of the duct. The W profile indicates the existence of secondary flow. The magnitude of the secondary flow is quite low (only about 1% of the bulk streamwise velocity), however, it has significant effects on the heat and momentum transport. The turbulent intensities at different locations are shown in Fig. 17. The rms values at the wall bisector are very much like those of turbulent channel flows or boundary layers. However, the flow behavior near the corner is totally different because of the presence of both walls. This result is instructive because we will compare our simulation results at wall bisector with DNS results of a channel later. Very good agreement with DNS and experimental results was obtained.
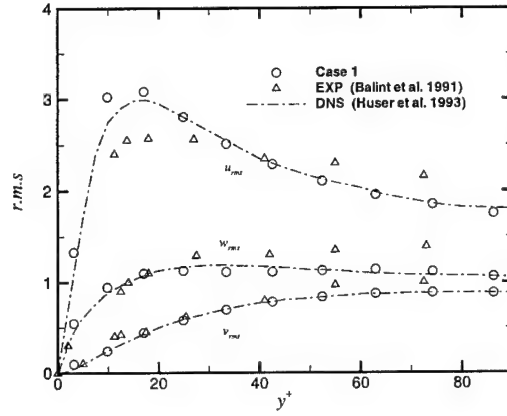
37

Figure 14: Turbulent intensities

The Heated Duct

The domain for the heated duct cases are the same as that of the isothermal cases which is shown in Fig. 11. Heat is applied to all four walls of the test section. Two different kinds of heating are considered: constant wall temperature (Cases 3, 5 and 6) and constant wall heat flux (Case 4). The computational details are in Table 1. Case 5 provides the highest heating level in these cases while Case 4 imposes a higher heating level than Case 3. The ratio of average wall temperature to the bulk temperature near the outlet for Case 3 is 1.13, 1.45 for Case 4, 1.53 for Case 5 and 1.14 for Case 6. Because the heated duct flows are non homogeneous in the x direction, the mean values of the statistical quantities are shown mostly for a streamwise location near the outlet (except the streamwise Nusselt number distribution) and are obtained by averaging only in time. Figure 18 shows the streamwise mean velocity profiles at the wall bisector. Here the mean velocity is normalized by the local friction velocity. For the same Reynolds number, the higher heating velocity profile departs more from the log-law. The mean temperature profiles are plotted in wall coordinates in Fig. 19. The mean temperature difference is given as

$$\Theta^+ = \frac{T_w - T}{T_\tau}$$
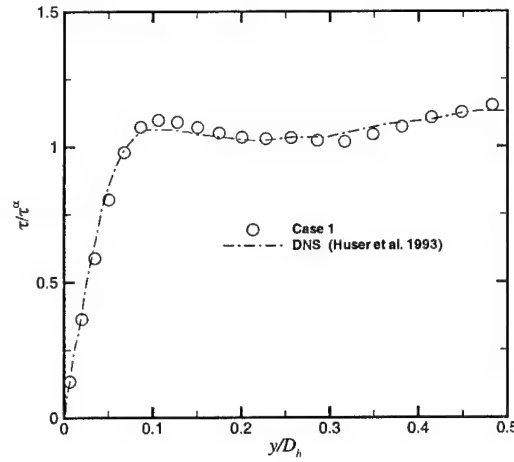$$T_\tau = \frac{q_w}{\rho_w c_p u_\tau}. \tag{84}$$

Figure 15: Local wall shear stress

Also the higher heating case departs from the thermal log-law more. This trend is consistent with what is observed in channel flow with heat transfer under variable property conditions [2]. Figure 20 shows the wall shear stress distributions normalized by the averaged wall shear stress. In the isothermal case, there is a local maximum stress at the mid-wall. Heating tends to suppress this mid-wall maximum. This is consistent with the results of one-side heated square duct cases [32]. Figures 21 and 22 show the variation of heat flux and temperature around the duct perimeter for Cases 3 and 4, respectively. The local heat flux is normalized by the average wall heat flux and the nondimensional temperature is defined as

$$\theta = \frac{T_w - \langle T_w \rangle}{T_\tau},$$ (85)

where $\langle T_w \rangle$ is the average wall temperature. The LES results of Pallares et al. [33] and experimental data of Brundrett et al. [34] are shown for comparison purposes. Our results agree with the LES results well and the discrepancy with experiment is probably attributable to the high Reynolds number the experiment employed ($Re = 75000$) which tends to smooth the heat flux distribution. The turbulent intensities at the wall bisector are shown in Figs. 23, 24 and 25. DNS results of a heated channel [35, 36] and a thermal boundary layer [37] are also shown for comparison. The velocity fluctuations of the low heating case agree with DNS results well. Higher heating decreases velocity fluctuations due to the increased thickness of the viscous sublayer. The temperature fluctuations of
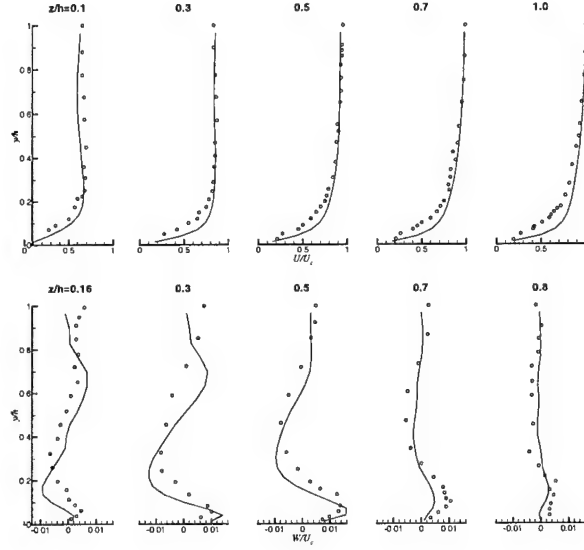
39

Figure 16: Mean velocity at different locations ——, Case 1; ○, Experiment (Cheesewright et al. 1990).

Case 3 are over predicted by the present simulations, especially the peak value. The reason is still not clear. However, the location where the maximum temperature fluctuation occurs for Case 5 is in good agreement with DNS data, which is $y^+ \approx 18$. The temperature fluctuations for the isoflux wall case agrees with DNS results very well. As the wall is approached, the rms temperature fluctuation becomes a constant 2.0 when very a thin wall is considered [38]. The distribution of streamwise Nusselt number is shown in Fig. 26. The Nusselt number is normalized by the fully developed (both velocity and temperature profile) Nusselt number Nu_{fd}. In the present work, the empirical equation

$$Nu_{fd} = 0.023 Re_b^{0.8} Pr^{0.4} \left(\frac{T_w}{T_b}\right)^{-0.55} \tag{86}$$

was used to estimate the reference Nusselt number. The series solution [39] and experimental results of Sparrow et al. [40] are also shown for comparison purposes. Good agreement has been obtained. Finally, the profiles of mean and rms velocities for a heated duct at different locations are shown in Figs. 27 and 28. Comparing with the isothermal duct, only the secondary flow shows some obvious differences, especially in the vicinity of the duct middle plane. This is because of the enhanced ejection around the wall bisector which is caused by wall heating. This is displayed on Fig. 29. This kind of phenomenon has also been confirmed by an experimental study [41].
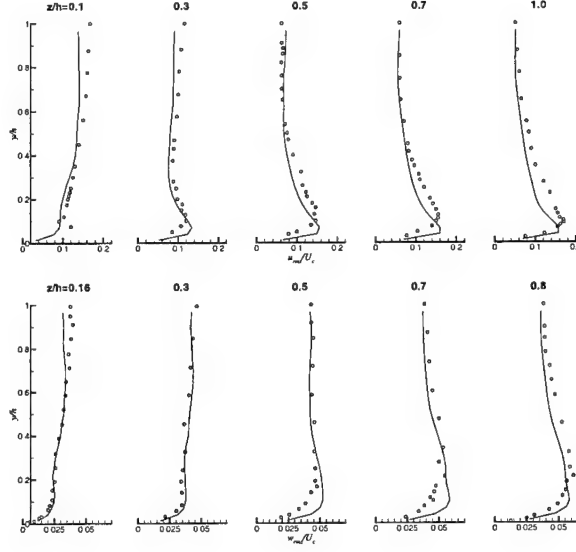
Figure 17: Turbulent intensities at different locations ———, Case 1;　　　　○, Experiment (Cheesewright et al. 1990).

4.3.2 Turbulent Heat Transfer in a Square Duct With Rotation

In a rotating frame, the flow will feel both Coriolis and centrifugal buoyancy forces. The source term in Eq. 38 becomes

$$\mathbf{S} = \begin{pmatrix} 0 \\ 2\rho Ro u_2 - \frac{Gr}{\varepsilon Re^2}\rho \\ -2\rho Ro u_1 \\ 0 \\ 0 \end{pmatrix}, \tag{87}$$

when the rotation is in z direction and x coordinate is aligned with the flow direction as Fig. 11 shows. The rotation number Ro is $Ro = \frac{\Omega D}{U_b}$ where Ω is angular velocity and U_b is the bulk velocity. The Grashof number, Gr, is defined as $Gr = -\frac{\rho_b^2 \beta (T_w - T_b)\Omega^2 r_m D^3}{\mu^2}$ where r_m is the mean rotating radius. Notice that r_m can be negative if the fluid flows inward toward the axis of rotation. Thus, the Grashof number is negative for outward flow and positive for inward flow under heating with the current Grashof number definition. ε is equal to $\beta(T_w - T_b)$. The computational details are in Table 2.
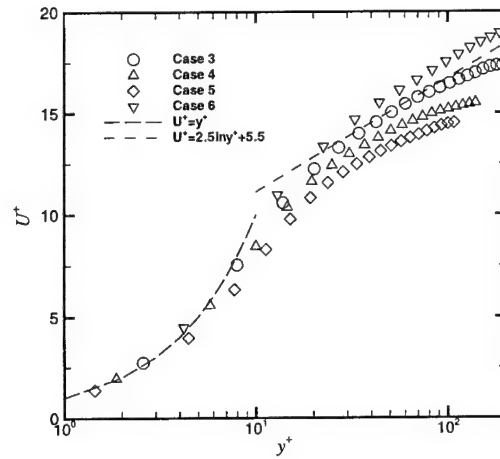
41

Figure 18: Streamwise mean velocity

Table 2: Computational details, cases with rotation

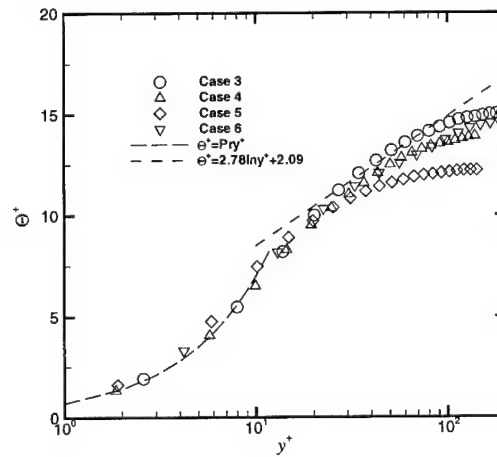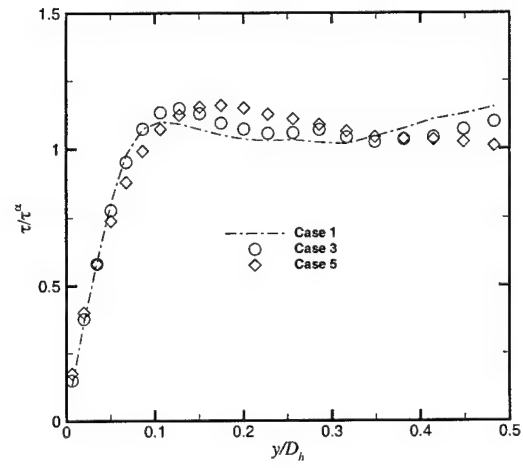| Case	Re_b	Ro_b	Grid Size	q_w	T_w/T_b	Gr
1	4,500	0.0133	$180 \times 40 \times 40$	0.0	1.0	0.0
2	4,500	0.0266	$180 \times 40 \times 40$	0.0	1.0	0.0
3	5,000	0.176	$240 \times 40 \times 40$	-	1.12	0.0
4	5,000	0.176	$240 \times 40 \times 40$	-	1.12	-2.2×10^6
5	5,000	0.176	$240 \times 40 \times 40$	-	1.12	2.2×10^6
6	5,000	0.176	$240 \times 40 \times 40$	6.4×10^{-4}	-	0.0
7	5,000	0.176	$240 \times 40 \times 40$	6.4×10^{-4}	-	-2.2×10^6
8	5,000	0.176	$240 \times 40 \times 40$	6.4×10^{-4}	-	2.2×10^6
9	5,000	0.088	$240 \times 40 \times 40$	6.4×10^{-4}	-	-2.2×10^6
10	10,000	0.088	$240 \times 40 \times 40$	1.1×10^{-3}	-	-2.2×10^6

Figure 19: Mean temperature

Figure 20: Local wall shear stress
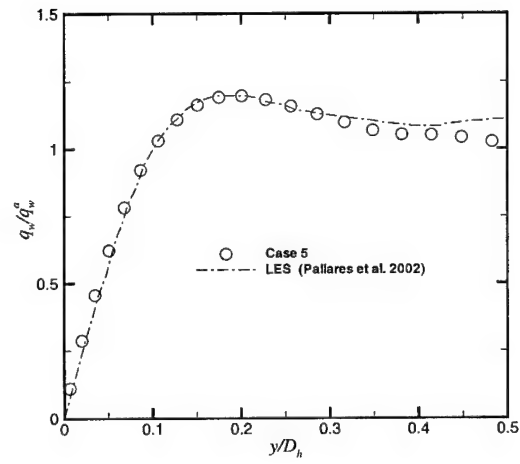
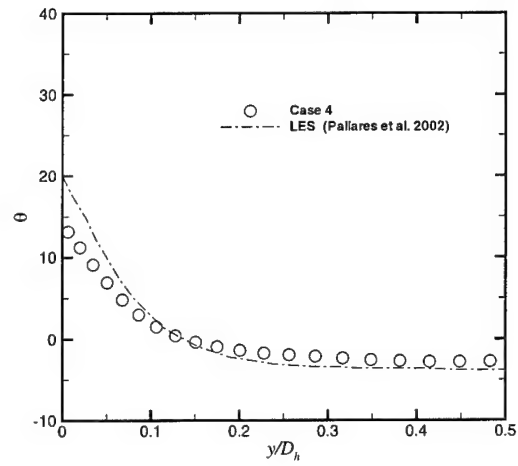

Figure 21: Local wall heat flux
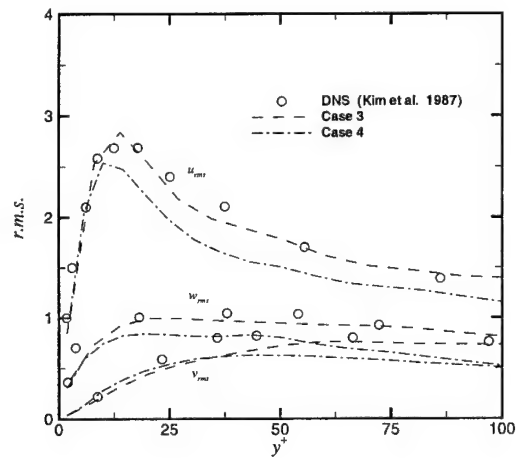
Figure 22: Local wall temperature

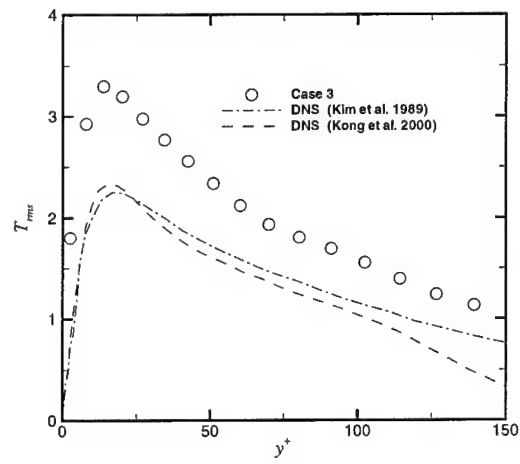Figure 23: Turbulent intensities: velocity

44

Figure 24: Turbulent intensity: temperature
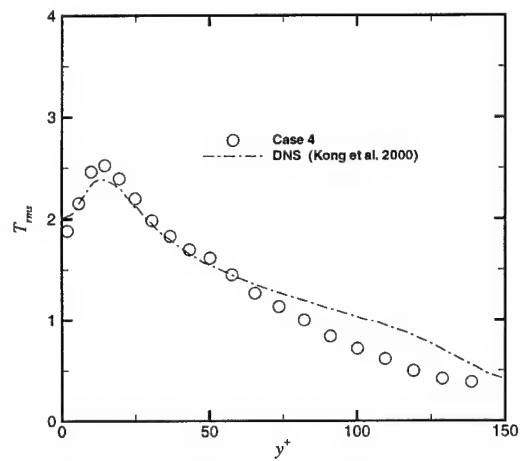
Figure 25: Turbulent intensity: temperature

45
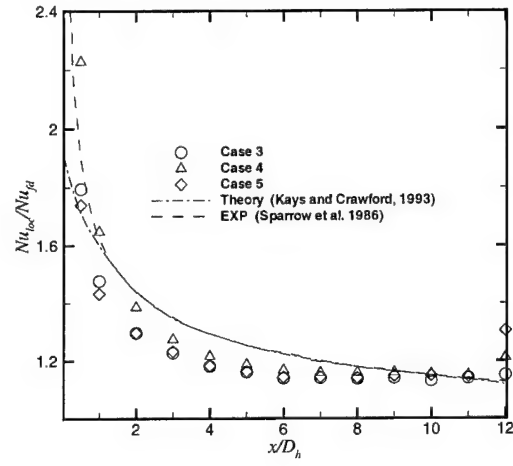
Figure 26: Local Nusselt number distribution
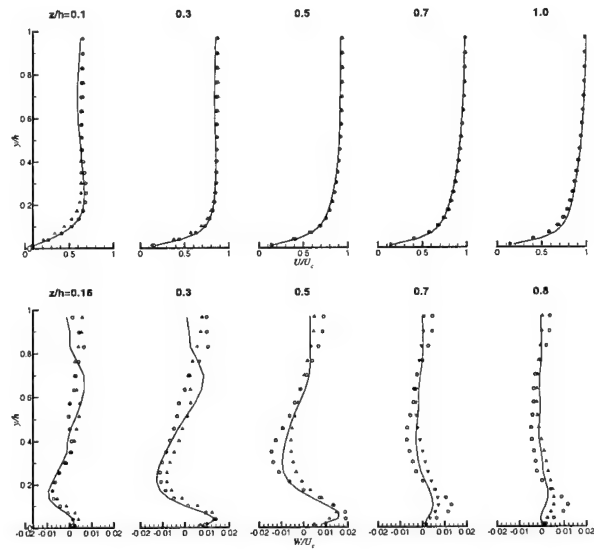
Figure 27: Mean velocity at different locations ——, Case 1;   o, Case 3;   Δ, Case 4.

Figure 28: Turbulent intensities at different locations ——, Case 1;   o, Case 3;   Δ, Case 4.

Hot fluid ejection

Figure 29: Instantaneous transversal vector field
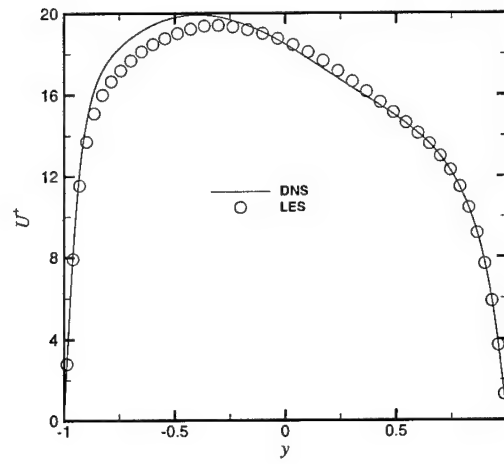
Figure 30: Streamwise mean velocity
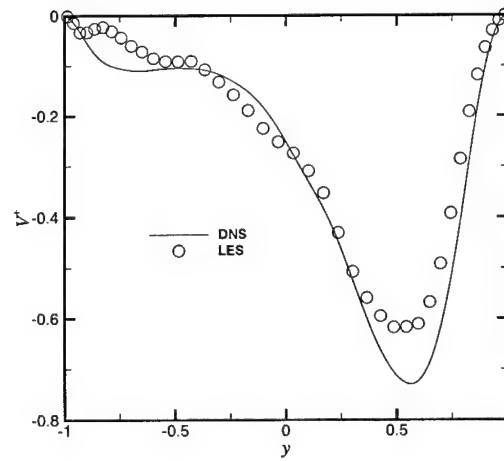
Figure 31: Secondary velocity

48
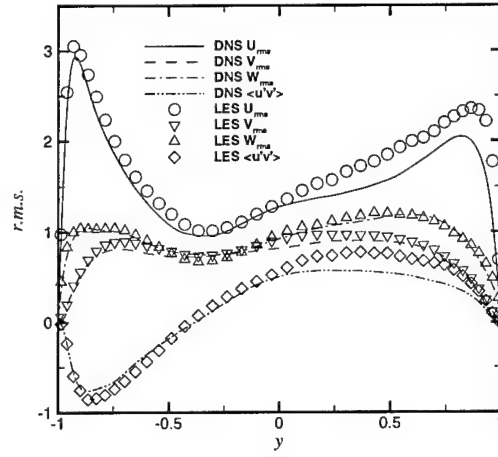
Figure 32: Turbulent intensities
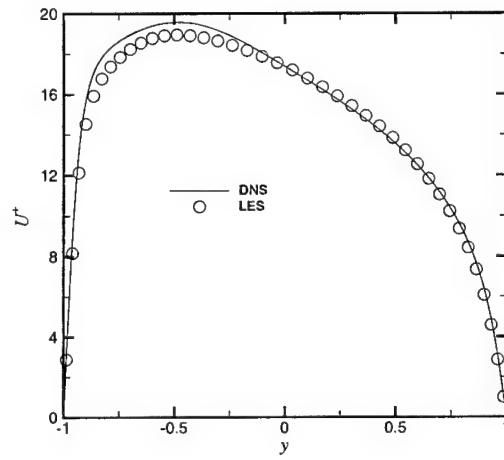
Figure 33: Streamwise mean velocity

49
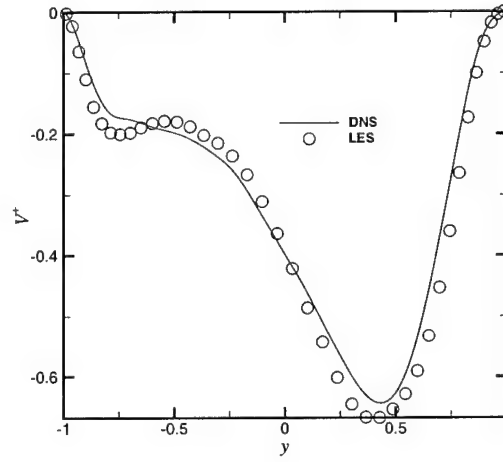
Figure 34: Secondary velocity
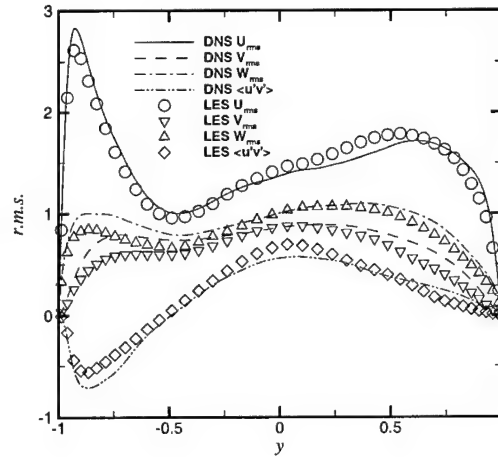
Figure 35: Turbulent intensities

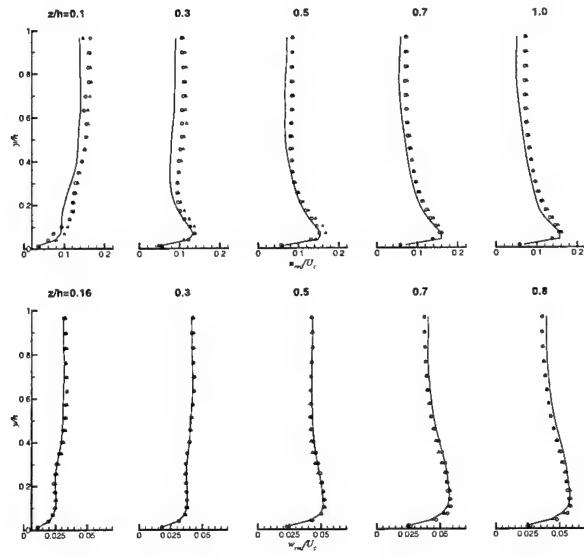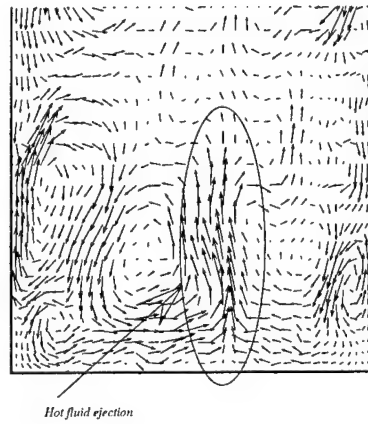Two isothermal rotating duct cases (Cases 1 and 2) were used to validate our code. The results of mean profile and velocity fluctuations at wall bisector B (see Fig. 11) are compared with DNS results [42] (see Figs. 30-35). Very good agreement has been obtained. The secondary velocity vector and streamwise velocity contours are also shown (see Fig. 36 to Fig. 38). It can be seen from the above results that the Coriolis force generates persistent secondary flows as well as increase/decrease in the mean shear stress ($\frac{\partial U}{\partial y}$) and turbulent intensities at the unstable/stable side, respectively. The modification of the mean shear stress is, from another viewpoint, the shift of the axial flow toward
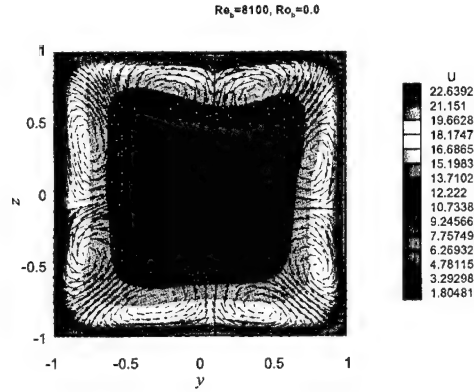
Figure 36: Secondary flow pattern and streamwise velocity distribution

the unstable side. When the rotation number is high (see Fig. 38), the profile of U becomes uniform in the z direction, which is known as the Taylor-Proudman effect. This phenomenon is a result of the balance between pressure gradient and Coriolis force, which has no component in the z direction.

Then heated rotating duct cases were simulated. Two heating conditions, constant wall temperature and constant wall heat flux, were considered. Due to rotation, the secondary flow transports the central cold fluid to the unstable side which results in relatively lower local temperatures at the unstable side and higher temperatures at stable side. Density differences arise as a consequence of these local temperature differences. The buoyancy contributes in the aiding/opposing directions to the mean flow at the unstable/stable sides, respectively, if the Grashof number is negative (outward flow), which helps in shifting the axial flow toward the unstable side caused by Coriolis force, and the situation is reversed for inward flow (positive Grashof number). This effect can be seen from Figs. 39 and 40 which show mean streamwise velocity profiles at the wall bisectors of the forced and mixed convection cases. Also we can see that the buoyancy force causes the flow to separate at the stable side when the negative Grashof number is large enough (Case 7) in magnitude. Such a mechanism is depicted in Fig. 43. The mean temperature profiles at the wall bisectors of different heated cases are shown in Figs. 41 and 42. The nondimensional temperature is defined as

$$\theta = \frac{\langle T_w \rangle - T}{\langle T_\tau \rangle},$$
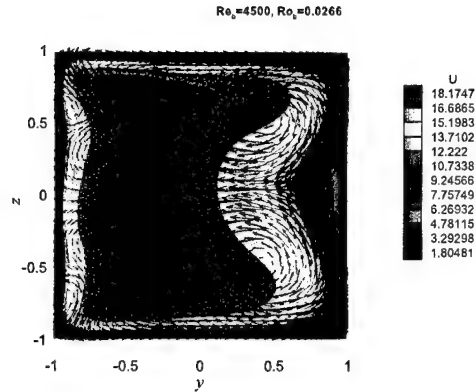(88)

51

Figure 37: Secondary flow pattern and streamwise velocity distribution

where $\langle T_w \rangle$ is the average wall temperature and $\langle T_\tau \rangle$ is the average friction temperature. In comparison of the buoyancy-free flows, a significant temperature rise appears near the stable side for outward flows due to the slower reversed fluid movement caused by the opposing buoyancy. Such a situation always reduces the heat transfer on the stable wall. However, this deterioration is somewhat compensated for by the enhanced turbulence level. Similar results have also been reported by Hwang et al. [46]. Steeper temperature profiles appear near the stable wall for inward flows.

As mentioned above, an important effect of rotation on a turbulent duct flow is the stabilization/destabilization of turbulence on walls normal to the rotation axis. This effect is a result of the modification of mean shear stress caused by the Coriolis force. The buoyancy force influences turbulent intensity in two ways: it modifies the mean shear further and takes part in the turbulent production term. The mean velocity fluctuation profiles along wall bisector B are shown in Figs. 44 and 45. In the outward flow, the turbulent intensity near the stable side is greatly enhanced by the buoyancy. This is because the reversed flow caused by buoyancy gives rise to a strong mean shear gradient near the stable wall. At the unstable side, there is also some turbulence intensity increase because of the growing mean shear gradient caused by the aiding buoyancy. In inward flow, the mean velocity fluctuation decreases/increases slightly at the unstable/stable side with the reduction/augmentation of mean shear gradients. The temperature fluctuation profiles along wall bisector B of different cases are shown in Fig. 46 and Fig. 47. Rotation decreases the temperature fluctu-
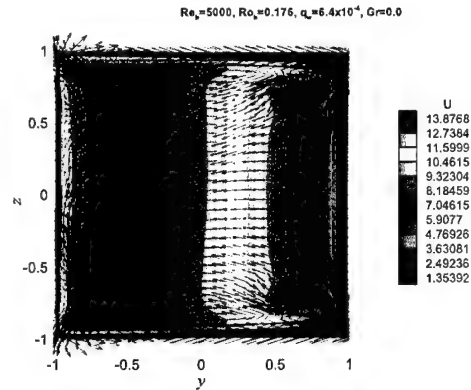
52

Figure 38: Secondary flow pattern and streamwise velocity distribution

ations near the stable wall because of the suppression of the turbulent heat fluxes. The buoyancy

for the outward flow (negative Grashof number) considerably increases the temperature fluctuation

intensity at the stable wall. The temperature fluctuation near the stable wall for inward flows also

increases somewhat because of the steeper temperature gradient caused by the aiding buoyancy.

The heat transfer coefficient is strongly affected by rotation. The Coriolis force shifts the axial

flow toward the unstable side which produces a thinner/thicker boundary layer at the unstable/stable

wall. Due to the thickness change of the boundary layers, the heat transfer coefficient at the un-

stable/stable wall increases/decreases. The buoyancy force aids this tendency for outward flows

(negative Grashof number) and hinders such tendency for inward flows (positive Grashof number).

This can be seen from Fig. 49. The comparison between numerical simulation and experiments

[45] is also given (Figs. 48 and 49). The agreement is fairly good and the discrepancy may be

attributed to the differences between the numerical and experimental settings. The heat transfer co-

efficient profiles for different rotation numbers and Reynolds numbers are given in Fig. 50 and 51.

With the same rotation number and Reynolds number, the isoflux cases show higher heat transfer

rates on both unstable and stable walls. With the same heating condition and Reynolds number, the

differences between heat transfer coefficients on unstable and stable walls increase with increasing

rotation number. With the same heating condition and rotation number, the Reynolds number has

little impact on the local heat transfer coefficients, which agrees well with the physical meaning of
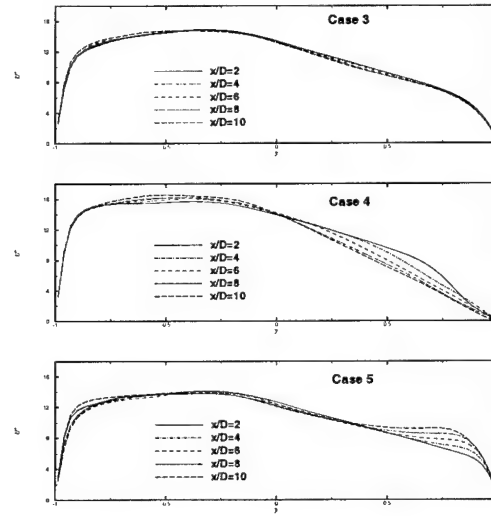
Figure 39: Streamwise mean velocity

rotation number (which is a measurement of the relative strength of the Coriolis force compared to the inertia force) and experimental results [44].
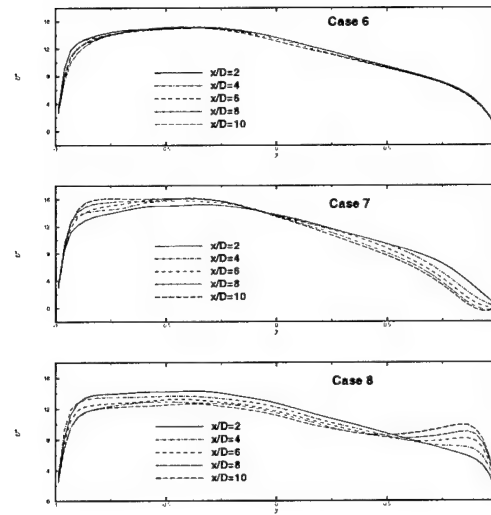
Figure 40: Streamwise mean velocity
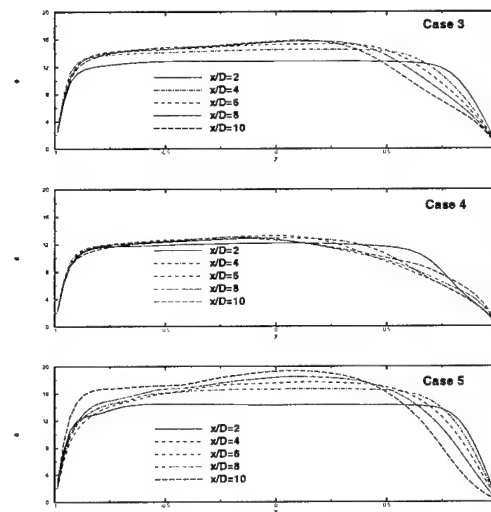
Figure 41: Mean temperature

55
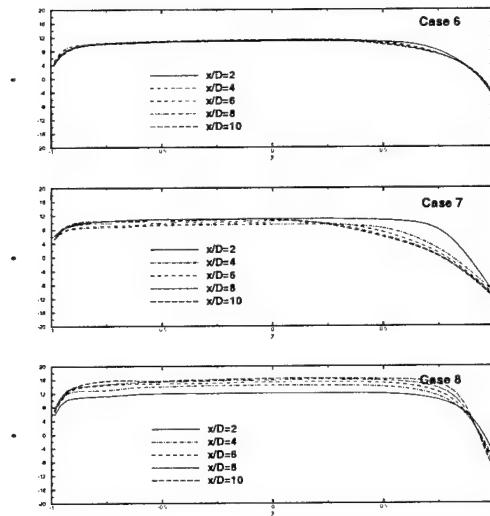
Figure 42: Mean temperature
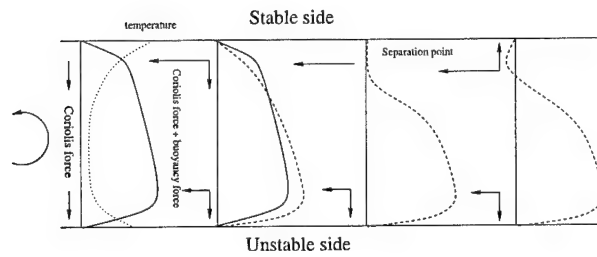
Figure 43: Sketch of the flow separation mechanism at the leading wall when $Gr < 0$
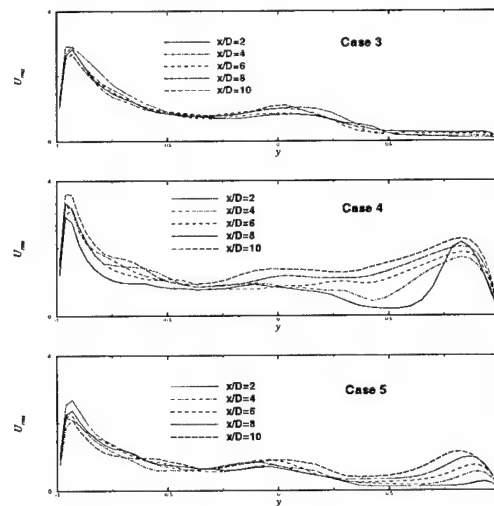
Figure 44: Turbulent intensity: velocity

56
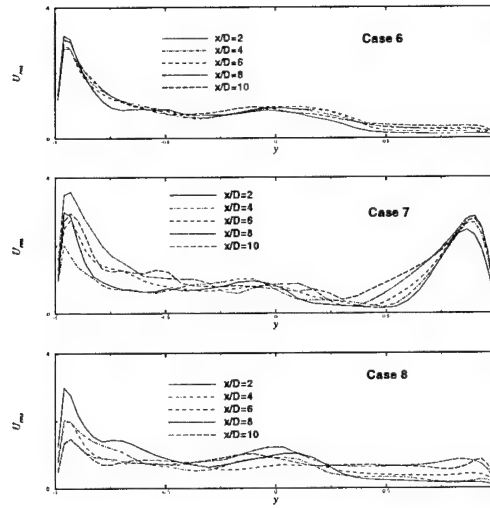
Figure 45: Turbulent intensity: velocity
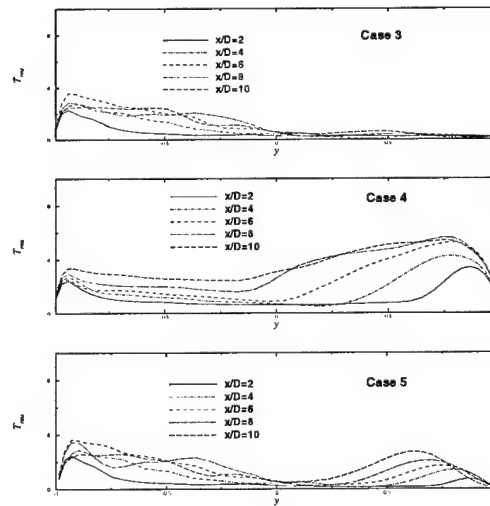
Figure 46: Turbulent intensity: temperature
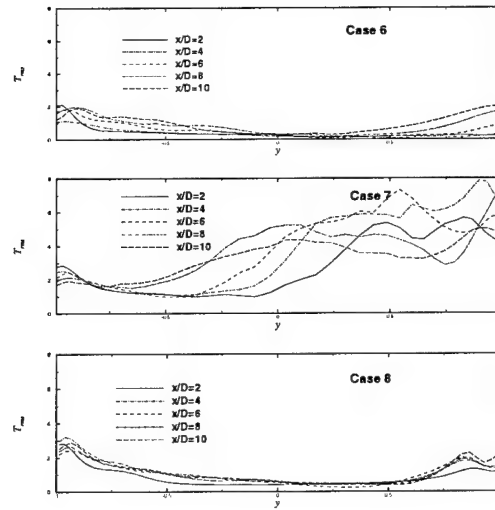
Figure 47: Turbulent intensity: temperature
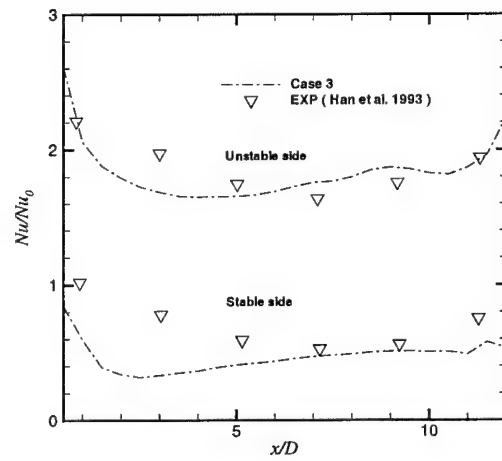
Figure 48: Streamwise Nusselt number distribution

58
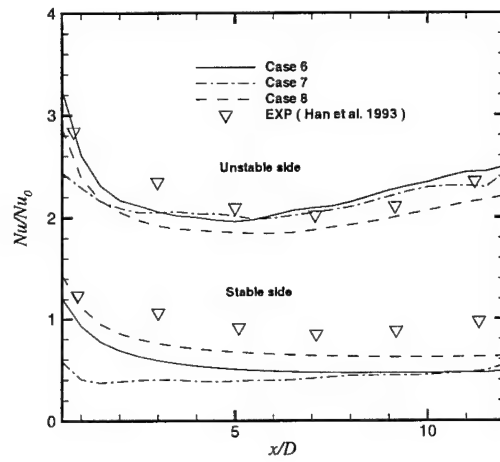
Figure 49: Streamwise Nusselt number distribution
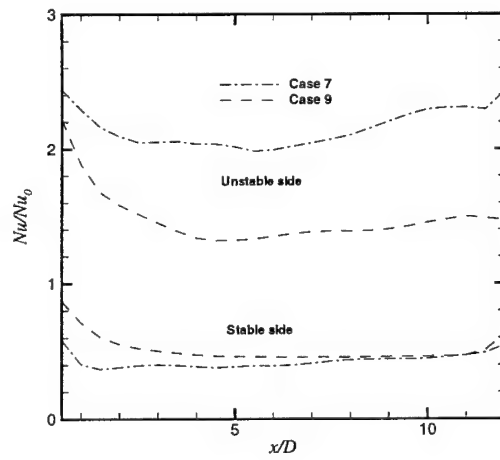
Figure 50: Effect of rotation number on streamwise Nusselt number distribution
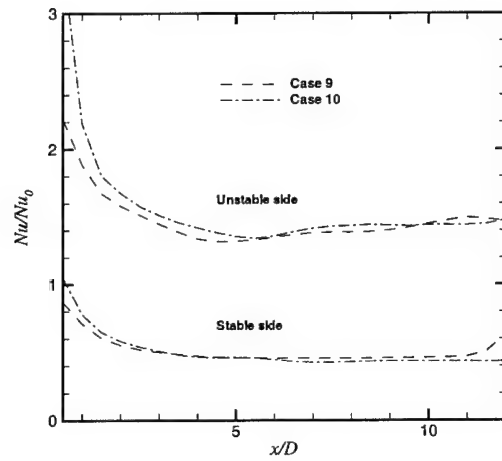
Figure 51: Effect of Reynolds number on streamwise Nusselt number distribution

5 External Turbulent Boundary Layers

5.1 Introduction

The successful simulation of film cooling of a turbulent flat plate flow subjected to free stream turbulence relies on the development of the following major techniques. First, a robust and efficient numerical solver designed for compressible flows is needed. Second, a technique is needed to generate appropriate inflow or starting conditions (including the freestream turbulence) that results in the development of a flow that captures the correct first, second and even higher order statistics. Third, it must be possible to accurately resolve the geometrically complex domain for the film cooling configuration. All of these subtasks are challenging. In this project we attempted to make several advances to this technology that are discussed in the following sections. First we focus on the external boundary layer.

5.2 Numerical Scheme

In order to simulate the compressible turbulent boundary layer, we formulated a new fractional step method. This method combines a preconditioning technique with a factorization treatment ror the Jacobian matrix so that the eigenvalues would cluster near one regardless of the Mach number, and the threefold coupling among temperature, pressure and velocities, from which the major numerical difficulties arise, would be decoupled. The applied factorization enables the resolved submatrices to be positive definite which guarantees the convergence of the iterative numerical procedure. The numerical formulation used in the research is based on a finite volume discreatiztion of the Favre-filtered compressible Navier-Stokes equations. Unlike the traditional fractional step method [47], which was designed for incompressible flows, this method offers a robust way to simulate compressible flows.

5.2.1 Quasi-Newton Iteration

The best-known and widely applied method for dealing with nonlinear equations is the Newton method. There are two main considerations for the Newton like methods, local convergence and global convergence. When the initial guess is sufficiently close to the solution, the Newton method,

e.g. Kantorovich method [48], has a quadratic convergence rate. Its convergence strictly depends on an appropriate initial guess, but such a guess is almost impossible for the simulation of complex flows. Alternatively, the quasi-Newton method, which offers a global convergence advantage, enables us to calculate the complex flows with a rough initial guess. But the price is the convergence rate. Unlike the local method, the quasi-Newton method has a superlinear convergence rate [48]. Superlinear means that the decay of the residual error is no less than a power function. For the simulation of complex flows involving turbulence, superlinear should be a satisfy convergence speed. In the quasi-Newton method, the Jacobian matrix will be adjusted by a factorization technique. In this section, we present a new factorization technique to achieve the global convergence.

Representing the Newton-like method applied to the governing equations by

$$J\delta v = -F \tag{89}$$

where J is the Jacobian matrix. Usually, for the discretized Navier-Stokes equations, such a Jacobian matrix may not be diagonally dominant, and the condition number may be very large, unless the very small time step is applied. But even so, in incompressible flows, the Jacobian matrix still may not be diagonally dominant. Therefore, the Jacobian must be adjusted. The main idea of the present approach is to search for a left multiplier P and a right multiplier M so that the updated solver becomes

$$PJMM^{-1}\delta v = -PF \tag{90}$$

Actually, the left multiplier is essentially a preconditioning matrix, and the right multiplier implements the factorization.

5.2.2 Preconditioning

The preconditioning matrix proposed by Pletcher and Chen [3] is utilized. It is

$$
P = \begin{pmatrix}
\dfrac{q}{RC_v} & -\dfrac{\hat{U}}{RC_v} & -\dfrac{\hat{V}}{RC_v} & -\dfrac{\hat{W}}{RC_v} & -\dfrac{1}{RC_v} \\[8pt]
-\dfrac{\hat{T}\hat{U}}{\hat{P}} & \dfrac{\hat{T}}{\hat{P}} & 0 & 0 & 0 \\[8pt]
-\dfrac{\hat{T}\hat{V}}{\hat{P}} & 0 & \dfrac{\hat{T}}{\hat{P}} & 0 & 0 \\[8pt]
-\dfrac{\hat{T}\hat{W}}{\hat{P}} & 0 & 0 & \dfrac{\hat{T}}{\hat{P}} & 0 \\[8pt]
\dfrac{\hat{T}}{\hat{P}}\left(\dfrac{q}{RC_v}-1\right) & -\dfrac{\hat{T}\hat{U}}{\hat{P}C_v} & -\dfrac{\hat{T}\hat{V}}{\hat{P}C_v} & -\dfrac{\hat{T}\hat{W}}{\hat{P}C_v} & \dfrac{\hat{T}}{\hat{P}C_v}
\end{pmatrix}
$$

where

$$
q = \frac{(\hat{U}^2 + \hat{V}^2 + \hat{W}^2)}{2}
$$

Multiplying both side of Eqs. (2), (3) and (4) with this preconditioning matrix, yields

$$
\begin{pmatrix}
\dfrac{D}{RDt} & b\dfrac{\partial}{\partial x} & b\dfrac{\partial}{\partial y} & b\dfrac{\partial}{\partial z} & 0 \\[8pt]
e\dfrac{\partial}{\partial x} & \dfrac{D}{Dt} & 0 & 0 & 0 \\[8pt]
e\dfrac{\partial}{\partial y} & 0 & \dfrac{D}{Dt} & 0 & 0 \\[8pt]
e\dfrac{\partial}{\partial z} & 0 & 0 & \dfrac{D}{Dt} & 0 \\[8pt]
0 & \dfrac{\hat{T}R\partial}{Cv\partial x} & \dfrac{\hat{T}R\partial}{Cv\partial y} & \dfrac{\hat{T}R\partial}{Cv\partial z} & \dfrac{D}{Dt}
\end{pmatrix}
\begin{pmatrix}
\delta P \\[8pt] \delta U \\[8pt] \delta V \\[8pt] \delta W \\[8pt] \delta T
\end{pmatrix}
=
\begin{pmatrix}
-f_1 \\[8pt] -f_2 \\[8pt] -f_3 \\[8pt] -f_4 \\[8pt] -f_5
\end{pmatrix}
$$

where $b = \dfrac{\hat{P}}{R} + \dfrac{\hat{P}}{C_v}$, $e = \dfrac{\hat{T}R}{\hat{P}}$, and vector $\vec{f} = P\vec{F}$. For simplification, it can be represented as

$$
\begin{pmatrix}
a & bD & 0 \\[6pt]
eG & C & 0 \\[6pt]
0 & B & E
\end{pmatrix}
\begin{pmatrix}
\delta P \\[6pt] \delta V_i \\[6pt] \delta T
\end{pmatrix}
=
\begin{pmatrix}
-f_1 \\[6pt] -f_i \\[6pt] -f_5
\end{pmatrix}
\tag{91}
$$

where G is the gradient operator, D is the divergence operator, $a = \dfrac{D}{RDt}$, $\delta V_i = \begin{bmatrix} \delta U & \delta V & \delta W \end{bmatrix}^{-1}$,

$f_i = \begin{bmatrix} f_2 & f_3 & f_4 \end{bmatrix}^{-1}$, $E = \dfrac{D}{Dt}$,

$$
B = \begin{bmatrix} \dfrac{\hat{T}R\partial}{Cv\partial x} & \dfrac{\hat{T}R\partial}{Cv\partial y} & \dfrac{\hat{T}R\partial}{Cv\partial z} \end{bmatrix}
\tag{92}
$$

63

and

$$C = \begin{pmatrix} \frac{D}{Dt} & 0 & 0 \\ 0 & \frac{D}{Dt} & 0 \\ 0 & 0 & \frac{D}{Dt} \end{pmatrix} = \frac{D}{Dt}I \qquad (93)$$

Here, $\frac{D}{Dt}$ is a material derivative and I is the identity matrix. Such a preconditioning matrix offers two advantages. First, it transfers the large off-diagonal terms into diagonal part so that the numerical scheme becomes more robust regardless of how small the Mach number is. Second, this preconditioning technique enables us to decouple the temperature and velocities. Clearly, the three-fold correlations among temperature, pressure and velocities produce some numerical difficulties especially in the low Mach flows.

According to a perturbation analysis,

$$\delta P = R\rho\delta T + RT\delta\rho$$

Under the reference system applied in this work, $R = \frac{1}{\gamma M_{ref} M_{ref}}$. This implies that a small perturbation on temperature will be greatly magnified by R, and be brought into the momentum equations by δP. Moreover, the eigenvalues after preconditioning are U and

$$[U(1+R) \pm \sqrt{U^2(R-1)^2 + 4R\alpha^2}]/(2R) \qquad (94)$$

where $R = \frac{\gamma}{M^2}$ and α is non-dimensional acoustic speed, $\alpha = \sqrt{\gamma RT}$. Obviously, those eigenvalues cluster near 1. Before preconditioning, they are U and $U \pm \alpha$. But it is still possible to have zero or negative eigenvalues in the solver regardless of the Mach number. In subsonic flows, $U < \alpha$, then $U(1+R) < \sqrt{U^2(R-1)^2 + 4R\alpha^2}$. In supersonic flows near the wall region, the local velocity U must be less than the acoustic speed α. In this region, $U(1+R) < \sqrt{U^2(R-1)^2 + 4R\alpha^2}$ also. With negative eigenvalues the iteratilve system is not positive definite. Such non positive eigenvalues can lead to difficulty with the quasi-Newton solver, and even cause the divergence of the iterative scheme. Therefore, a proper factorization technique needs to be developed.

5.2.3 Fractional Step Factorization

Denote the matrix M^{-1} in Eq.(90) as

$$
M^{-1} = \begin{pmatrix} a - bDC^{-1}eG & 0 & 0 \\ C^{-1}eG & I & 0 \\ -E^{-1}BC^{-1}eG & 0 & 1 \end{pmatrix}
\tag{95}
$$

where I is an identity matrix. Hence, the Jacobian matrix in Eq. (91) can be decomposed into

$$
\begin{pmatrix} 1 & bD & 0 \\ 0 & C & 0 \\ 0 & B & E \end{pmatrix} \begin{pmatrix} a - bDC^{-1}eG & 0 & 0 \\ C^{-1}eG & I & 0 \\ -E^{-1}BC^{-1}eG & 0 & I \end{pmatrix} \begin{pmatrix} \delta P \\ \delta u_i \\ \delta T \end{pmatrix} = \begin{pmatrix} -f_1 \\ -f_i \\ -f_5 \end{pmatrix}
\tag{96}
$$

Essentially, this decomposition is a fractional step procedure. Its efficiency arises from decoupling the velocities, pressure and temperature.

5.2.4 Numerical Procedure

Hence, the full discrete scheme can be represented as

$$
\begin{pmatrix} 1 & bD' & 0 \\ 0 & C' & 0 \\ 0 & B' & E' \end{pmatrix} \begin{pmatrix} a' - bD'\Delta t eG' & 0 & 0 \\ \Delta t eG' & I & 0 \\ -\Delta t \frac{\hat{T}R}{Cv}D'\Delta t eG' & 0 & I \end{pmatrix} \begin{pmatrix} \delta P \\ \delta u_i \\ \delta T \end{pmatrix} = \begin{pmatrix} -f_1 \\ -f_i \\ -f_5 \end{pmatrix}
\tag{97}
$$

As mentioned above, such a decomposition, essentially, is a fractional step procedure. It provides an efficient way to decouple velocities, pressure and temperature. The corresponding numerical procedures are:

1. Resolve

$$
C'\delta W_i = -f_i
\tag{98}
$$

for δW_i using an iterative scheme.

2. Substitute δW_i into equations

$$\delta p' = -f_1 - bD'\delta W_i \tag{99}$$

$$\delta T' = (-f_5 - B'\delta W_i)/E' \tag{100}$$

to obtain $\delta p'$ and $\delta T'$

3. Resolve the parabolic equation

$$(a' - \Delta t bD'eG)\delta P = \delta p' \tag{101}$$

for δP.

4. Obtain velocities by

$$\delta u_i = \delta W_i - C^{-1}eG\delta P \tag{102}$$

5. Obtain the temperature correction by

$$\delta T = \delta T' + E^{-1}BC^{-1}eG\delta P \tag{103}$$

This is a 5 step procedure. Except steps 1 and 3, all of the other steps can be solved non-iteratively. In step 1, C' is discretization of C; therefore, a small enough time step Δt will provide the diagonal dominance, which should guarantee the convergence of step 1. In the traditional factional step method, the equation to be solved in step 3 is a Poisson equation

$$\Delta\delta P = RHS \tag{104}$$

But in compressible flow, the equation is not a Poisson equation, but a parabolic equation. Recall that $b = \frac{\hat{P}}{R} + \frac{\hat{P}}{C_v}$, $e = \frac{\hat{T}R}{\hat{P}}$ and $a = \frac{D}{RDt}$. Equation (101) is the discretization of following equation:

$$\frac{D\delta P}{RDt} - \Delta t(\frac{\hat{P}}{R} + \frac{\hat{P}}{C_v})\nabla(\frac{\hat{T}R}{\hat{P}}\nabla\delta P) = \delta P' \tag{105}$$

66

The above equation can be written as

$$c_1\frac{\partial \delta P}{\partial t} - \Delta\delta P - (\nabla\delta P)\cdot(\nabla\frac{\hat{\bar{T}}R}{\hat{\bar{P}}}) + c_1(u\cdot\nabla)\delta P = c_2\delta P' \tag{106}$$

where $c_1 = \frac{C_v}{\hat{\bar{P}}(R+C_v)\Delta t}$ and $c_2 = \frac{RC_v}{\hat{\bar{P}}(R+C_v)\Delta t}$.

By the factorization above, the parts which need to be solved iteratively are step 1 and step 3. Obviously, the associated Jacobian matrices are positive definite, and diagonally dominant. Therefore, they can be solved by iterative scheme efficiently.

5.3 A Generation Technique for the Turbulence in Turbulent Boundary Layers

In order to generate turbulence, we developed a dynamic adjustment technique for the inflow conditions to establish a turbulent boundary layer [51]. In 1988, Spalart [52] introduced a scaled periodic boundary condition method to produce the inlet profile of spatial evolving turbulent boundary layers. Lund *et al.* [53] further developed this concept. In their implementation, instantaneous profiles at a specific station were recycled to the inlet at each numerical step after rescaling. This rescaling was based on the similarity laws of the boundary layer, the law of the wall in the inner part and the defect law in the outer part of boundary layer. Kong *et al.*[37] applied Lund *et al.*'s idea to temperature, and formulated an inlet generator for turbulent thermal boundary layers. Their simulation results showed that this treatment also works well for the energy equation when fluid properties can be assumed to be constant.

For a simulation not stating from a proper initial condition, the above rescaling treatments may lead to a decrease of skin friction [54] with increasing time. Since the mean profiles are adjusted with the fluctuations synchronously, the flow keeps transferring its energy to small structures, and most of this energy eventually goes to the very small eddies and is dissipated. In the early part of the simulation, if the large eddy structures have not been correctly produced, the flows will not contain enough energy to sustain the turbulence. Finally, the skin friction will drop down to the value characteristic of laminar flows. To avoid this, Lund *et al.* [53] suggested making a correction to the solved velocities during the early part of simulation. Spille-Kohoff and Kaltenbach [54] suggested adding a source term to the resolved equation based on the desired Reynolds stress.

For solving this problem, we suggest replacing the traditional rescaling method with a dynamic
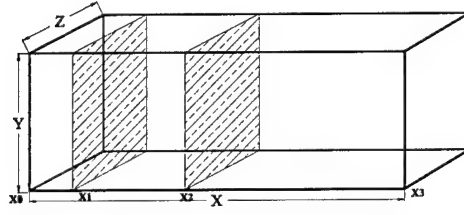
Figure 52: The configuration for a turbulent boundary layer and the recycling downstream station, which is dynamically selected by Eq. (107)

adjustment recycling method. This idea come from the observation that the structures in a turbulent boundary layer convect downstream with a speed proportional to the streamwise mean velocity. The proposed recycling method, namely the dynamic adjustment method,can be represented by

$$X_{rec} = X_1 + \min(X_{tag} - X_1, \alpha U_b max(0, (t - t_0)))$$ (107)

where X_{rec} is recycling location. X_{tag} is the desired recycling station when the numerical domain is completely filled by the turbulent structures produced by inflow.condition, X_1 is the starting location, t is non-dimensional time, U_b is the bulk velocity and t_0 is the time in which the leading edge of the convected flow generated at the inlet can reach station X_1. Equation (107 means that the recycle plane stays at station X_1 from $t = 0$ up to $t = t_0$, when the convective structures generated by the inlet condition is supposed to have passed though station X_1 except for the viscous sublayer, and then the recycle plane moves downstream with the speed αU_b until it reaches the location of the desired recycle station X_{tag}. After that, the recycle plane will stay fixed for the the rest of the calculation. This dynamic adjustment procedure is designed to keep the recycle plane inside the region influenced by the inlet conditions to achieve steady first and second order statistics. The reason for this is that if the initial condition is not proper, i.e. the correct large eddies do not appear in the flow, the mean profile and velocity rms profiles may be deformed, and similarity law cannot be applied. However,the similarity laws are the basis of rescaling method. Coupling of initial and inlet boundary condition may lead to the decay of skin friction. Therefore, Lund *et al.* suggested a correction to velocity profiles during the early part of simulation. This kind of correction may create some convergence problems. And the physical basis for this is not clear. In our work, we propose a

68

dynamic adjustment as a remedy for this problem.

As part of the validation procedure a case was computed for a Reynolds number based on the displacement thickness, Re_d, of 2000 using a numerical domain $X \times Y \times Z = 84\delta_d \times 30\delta_d \times 19.2\delta_d$, and a numerical grid of $n_i \times n_j \times n_k = 280 \times 80 \times 120$, and a Mach number of 0.06. The time step was 0.2. A dynamic SGS model was applied.

Figure 53: Comparison of streamwise mean profile in a turbulent boundary layer in the order of increasing streamwise direction; the units of X is one initial displacement thickness
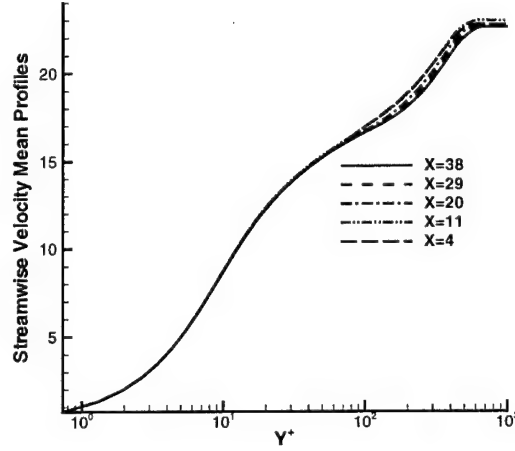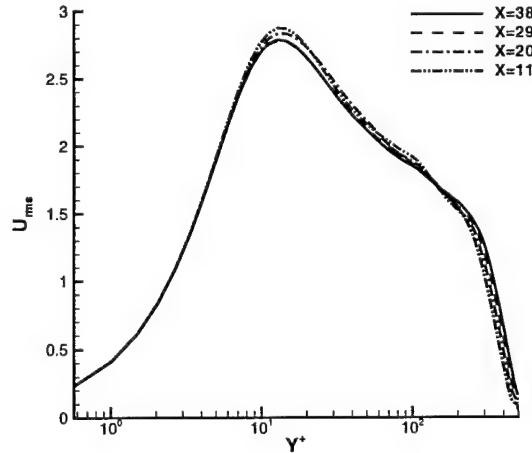
Figure 54: Comparison of U_{rms} profile in a turbulent boundary layer in the order of increasing streamwise direction; the units of X is one initial displacement thickness

The streamwise mean profiles at different streamwise stations are compared in Fig. 53. And

69

the U_{rms} profiles are shown in Fig. 54 in the order of increasing streamwise direction. From those figures, we observe that, with this dynamic inlet generation technique, the inlet buffer zone becomes fairly short, and the influence of buffer zone on the first and second order statistics is very small.

5.4 Simulation of a Turbulent Boundary Layer Subjected to Free Stream Turbulence

For the turbulent boundary layers subjected to free-stream turbulence, the transported energy from free stream to boundary layer will increase skin friction (Blair [55], Hancock and Bradshaw [56]). This relation was formulated as

$$\frac{\Delta C_f}{Cf_0} \propto \frac{Tu_e}{2+L/\delta}$$

This formula implies that a smaller turbulent free stream length scale makes a larger contribution to skin friction compared with a larger turbulent free stream length scale. Since shear is not large in the free stream, there is not much turbulent production there; therefore, the main feature in the free stream is dissipation. Length scale is a parameter related to the intensity of dissipation. Usually, grid turbulence has a length scale range from $10\delta_d$ to $50\delta_d$ (Barrett and Hollingsworth [57], [58]). In this range, the dissipation of free stream turbulence is very strong. Therefore, the mean profile in the wake region of a turbulent boundary does not change slowly in the downstream direction as is the case without free stream turbulence. In the other words, the defect law does not apply with free stream turbulence. Those features are extremely interesting, but very difficult to capture in the numerical simulations.

In order to describe this phenomena, we decompose the velocity into

$$U_{inlt}^{inner}(y_{inlt}^+) = \overline{U} + A(x,\eta)u_p(x,\eta,z,t) \tag{108}$$

$$U_{inlt}^{outer}(\alpha_{inlt}) = (\gamma_1 U_{recy}(\alpha_{inlt}) + \gamma_2 U_{recy}'(\alpha_{inlt},z,t)) + (1-\gamma_1)U_{ref} \tag{109}$$

$$U_{inlt}^{free}(\alpha_{inlt}) = \gamma_3 \left(\sum_{0 \le i \le m} Weight_i U_{recy_i}' \right) + U_{ref} \tag{110}$$

70

where the inner part ranges from 0 to 30 in the y^+ sense. Spalart's [52] inlet solver was applied for the inner part because the correlation of free stream turbulence and skin friction was successfully formulated by experiments. Experimental results show that Cebeci & Bradshaw's [59] mean velocity profile works in the inner part. If the free stream turbulence level is less than 12.5%, rms profiles without free stream turbulence can be applied. Therefore, Spalart's [52] inlet solver can be safely utilized as long as free stream turbulence level is lower than 12.5%.

But the profiles at the outer part of boundary layer are more complex. We take advantage of Lund *et al.*'s [53] outer part treatment, but the coefficient is different,

$$\alpha_{inlt} = \frac{\delta_{inlt}}{\delta_{99}} y_{recy} \tag{111}$$

where δ_{inlt} is the desired inlet boundary layer thickness, and δ_{99} is the boundary thickness located at recycle plane. In [53] γ was the weighting factor for the outer part of boundary layer associated with the defect law. Since the defect law does not work here, γ_1 was chosen such that the inner part and outer part was continuous in the mean velocity, i.e.

$$\gamma_1 = \frac{\overline{U}(y^+ = 30)}{U_{recy}(y^+ = 30)} \tag{112}$$

γ_2 was chosen such that rms velocity profile was continuous at the edge of boundary layer, i.e.

$$\gamma_2 = \frac{TU}{U_{recy}^{rms}(y = \delta)} \tag{113}$$

where TU is the free stream turbulent level.

Equation (110) represents our treatment of free stream turbulence. We need to maintain the free stream turbulence level and the turbulent length scale. Since the free stream does not contain turbulent production, small eddies decay faster than the larger eddies. Thus, at the different downstream stations, the ratio of energy contained by small eddies and the energy contained by large eddies are different. When the scaled periodic boundary condition is utilized, we cannot obtain a perfect inlet profile by only recycling a single downstream plane because that ratio is variable. So we recycle several planes, and use those planes to produce our inlet free stream profile. In Eq. (110), *weight$_i$*

71

Table 3: Weightings for Eq. (110)

Station	Location	Weighting
1	$x = 0.8\delta$	1.0/1.75
2	$x = 1.6\delta$	0.5/1.75
3	$x = 8.0\delta$	0.25/1.75

are weight functions that monotonically decrease in the order of increasing downstream distance,

$$\sum_{0 \leq i \leq m} Weight_i = 1 \tag{114}$$

and γ_3 is a coefficient such that the TU is maintained in the inlet profile. This we call a multi-level recycling method. The weighting function used in this work is given in Table 3. where 3 stations were applied in our calculation. Such a weighting was chosen so that the target length scale would be approached.
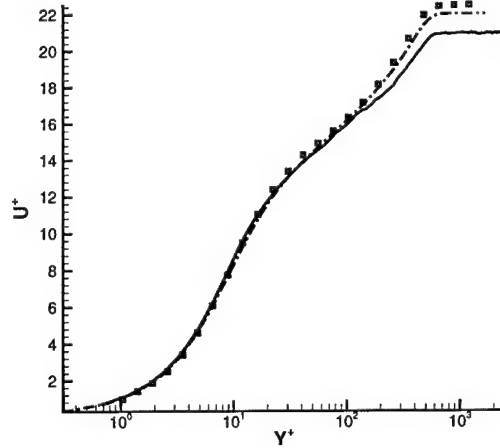
Figure 55: Comparison of mean velocity profile in a turbulent boundary layer $Re_{\delta_d} = 2000$, $TU = 5\%$ and $T_w = T_{ref}$; the solid line is LES results, the dashed line gives a DNS profile by Spalart [52] and the square symbols are experimental data by DeGraaff and Eaton [60]

Turbulent boundary layers ranging from $Re_d = 1800$ up to $Re_d = 2150$ were calculated by a dynamic subgrid model proposed by Germano *et al.* [61]. The simulated free stream turbulent level was 5%. Figure 55 shows the comparison of mean velocity profile in a turbulent boundary layer for $Re_{\delta_d} = 2000$ and $TU = 5\%$ and DNS profile calculated by Spalart [52] and an experimental profile by DeGraaff and Eaton [60]. Those DNS and experimental data are all on $Re_{\delta_d} = 2000$, but
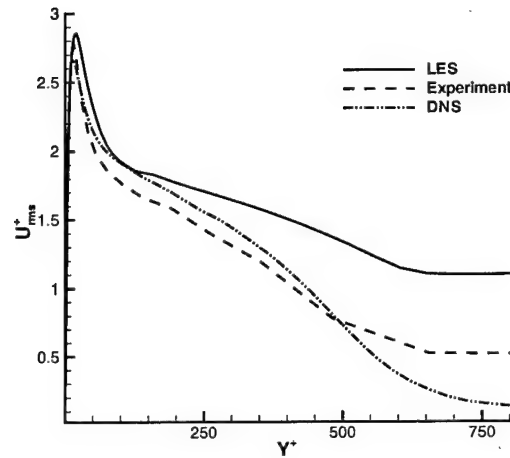
72

Figure 56: Comparison of streamwise *rms* profiles in a turbulent boundary layer $Re_{\delta_d} = 2000$, $TU = 5\%$ and $T_w = T_{ref}$ The DNS results are from Spalart [52] and the experimental data are from DeGraaff and Eaton [60]

without free-stream turbulence. The LES results in Fig. 55 exhibit almost the same main velocity curve in the inner part of boundary layers as the DNS and experimental data with no free stream turbulence, but exhibit a larger difference in the wake part. These phenomena match generally with the experimental observations by Barrett and Hollingsworth [62], Blair [55] and Hancock and Bradshaw [56].

5.5 Effect of Free Stream Turbulence and Heat Transfer on Turbulent Boundary Layers

Several cases were calculated in order to illustrate the effect of free stream turbulence and heat transfer on the turbulent boundary layer. For all cases the Mach number was 0.06, and $Re_{\delta_d} = 2000$, where δ_d is the inflow displacement thickness. The velocities in Fig. 57 were normalized by the wall friction velocities. The figure shows the effect of the heated wall on the boundary layer developing with no free stream turbulence. With wall heating the boundary layer is thinner than for the adiabatic case and some deviation from the log law is noted. The numerical results show that heat transfer will reduce the skin friction, but the free stream turbulence will increase it. Figure 58 illustrates the effect of heat transfer (without free stream turbulence) and free stream turbulence (in adiabatic flow) to the skin friction and Stanton number. The empirical curve in the Fig. 58 is

73
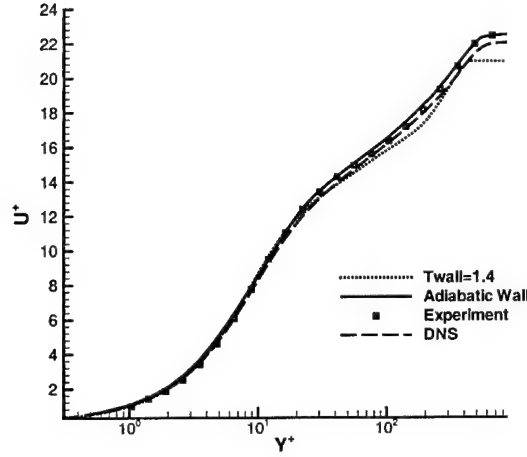
Figure 57: Comparison of mean velocity profiles in a turbulent boundary layer $Re_{\delta_d} = 2000$; the solid and dotted lines are LES results, the dashed line gives a DNS profile by Spalart [52] and the square symbols are experimental data by DeGraaff and Eaton [60]

$$Cf = 0.025Re_\theta^{-1/4} \tag{115}$$

where Re_θ is the Reynolds number based on momentum thicknes, and Tu stands for turbulence level. Subjected to the free stream turbulence with 5% turbulence level, the turbulence length scale, L, is $49\delta_d$ under the definition

$$L = -\frac{(u'^2)^{3/2}}{U}\frac{du'^2}{dx} \tag{116}$$

where δ_d is the inflow displacement thickness.

Figure 58: Comparison of C_f and St in a turbulent boundary layer

6 Film Cooling

This facet of our work is still in the code development and validation phase. The results to date look very promising, but additional simulations need to be completed before final conclusions can be drawn. The status of the work is discussed below.

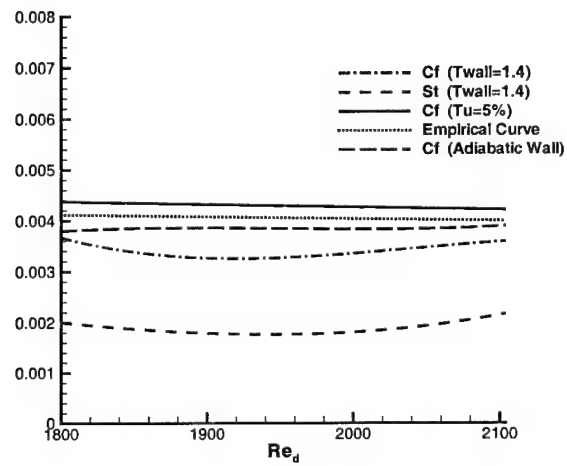The effect of the length of the coolant supply tube has received considerable attention in the literature. The tube L/D influences the tube discharge conditions and the resulting downstream structures. Goldstein et al. [63] found an appreciable difference in effectiveness between an $L/D =$ 5.2 and longer injection lengths. As the L/D increases, the discharge velocity profiles become more uniform. For a long tube, say $L/D > 6$, the discharge condition becomes nearly independent of tube entrance conditions.

Burd et al. [64] compared the film cooling effectiveness of an $L/D = 7.0$ configuration with one having $L/D = 2.3$. Their experiments showed that the short-hole injection flow penetrates farther from the wall and influences a greater extent of the region downstream from the hole under low free stream turbulence, but no significant differences in the normalized mean velocities were noted with high free stream turbulence.

Ligrani et al. [65] examined the film cooling effectiveness of a single row of film-cooling holes with and without compound angle orientations. They evaluated blowing ratios of 0.5, 1.0 and 1.5.

A long-tube configuration with $L/D = 8$ was selected for the first LES film cooling simulation. The blowing ratio was 0.5 and the density ratio, 2.0. The wall was adiabatic. The arrangement of the computational domain is shown in Fig. 59. The ratio of the diameter of pipe to the width of
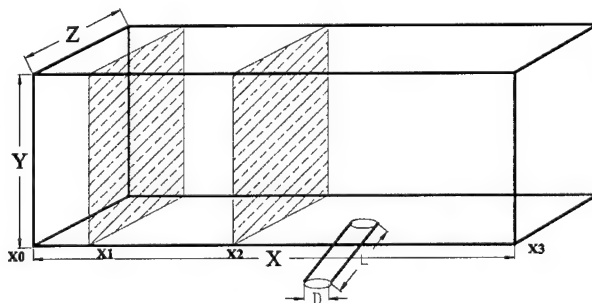

Figure 59: The numerical configuration for film cooling

boundary layer namely D/Z was 1/5. The ratio of the diameter of pipe to the boundary thickness, namely D/δ, was 0.44. The Reynolds number of the boundary layer ranged from 1800 up to 2700

based on the displacement thickness. The distance from inlet to the center of the coolant discharge hole was $56.5\delta_d$, where δ_d is displacement thickness, and the distance from the hole center to the outflow boundary was $72.5\delta_d$, which which corresponds to $22.656D$. The Reynolds number of the boundary layer at the discharge hold center was 2000. The Reynolds number for the pipe flow was 9357.1. The injection angle was 35°. The film cooling effectiveness was calculated according to

$$\eta = \frac{T_{a,w} - T_{r,\infty}}{T_{r,c} - T_{r,\infty}} \tag{117}$$

The grid was non-orthogonal in the tube and near the injection hole. Conservation was maintained by employing control volume concepts similar those employed with unstructured meshes. Figure 60 provides a downward view of the numerical mesh employed for the external boundary layer near the injection hole. Figure 61 shows the mesh in more detail.
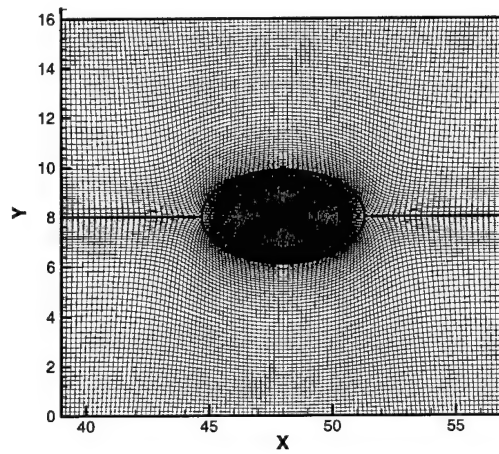
Figure 60: The computational mesh near the injection hole

Sixteen processors were used to calculate this case. The LU-SGS scheme and a dynamic SGS model were utilized. The numerical grid for the external turbulent boundary layer was $591 \times 85 \times 101$ corresponding to the streamwise, normal and spanwise directions, respectively. The numerical domain was $126 \times 22 \times 16$ in units of displacement thickness. The numerical grid was $241 \times 41 \times 101$ corresponding to streamwise, normal, and spanwise directions for the coolant supply pipe,respectively. The total number of control volumes used in the simulation exceeded 6 million. In units of the external boundary layer initial displacement thickness, the pipe radius was 1.6 and

77
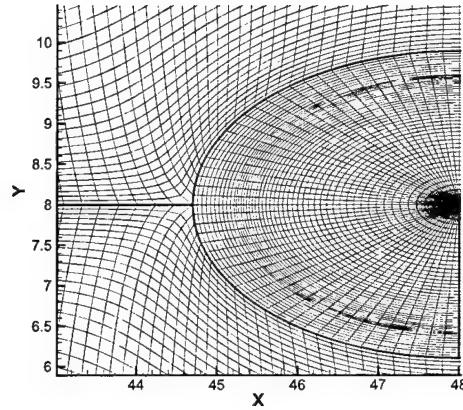
Figure 61: Expanded view of computational mesh near the leading edge of the injection hole

the length, 16.
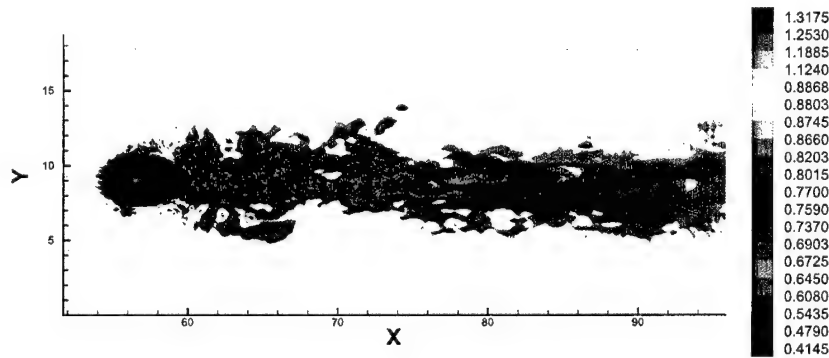
Figure 62: The downward view of instantaneous temperature contours at $y^+ = 14$; the units of the axes are displacement thickness, and the center of the hole is located at $x = 56.5$; Y represents the spanwise direction

Figure 62 shows the evolution of the coolant in the buffer zone of the turbulent boundary layer. Due to the strong turbulence in this region, the coolant mixes with the external flow very rapidly. Such mixing accelerates the energy transfer between the coolant and the surrounding flow.

Figure 63 shows the side view of the instantaneous temperature contours. This figure clearly shows the evolution of the coolant downstream. Although not discernable in the temperature field, the flow reverses immediately downstream of the hole. Such a reversed flow can be visualized as a vortex. The coolant reattaches to the wall just behind this vortex. The reattachment accelerated the

78

Figure 63: The side view of instantaneous temperature contours at the centerline of the numerical domain, the units of the axes are displacement thickness, and the center of the hole is located at $x = 56.5$
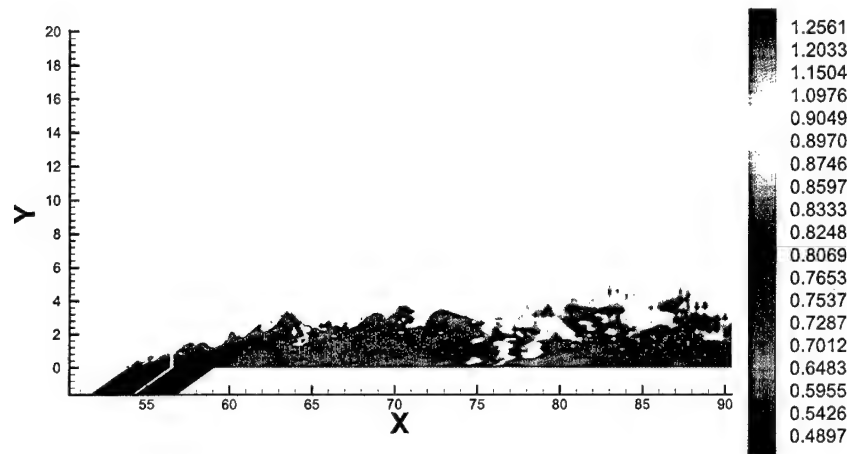
mixing.

Figure 64 shows the distribution of adiabatic effectiveness on the flat plate. In this case, the Reynolds number of the external turbulent boundary layer ranges from 1800 to 2300 based on displacement thickness, the density ratio is 2.0, and the blowing ratio is 0.5. The free stream turbulence level is zero in this case. Figure 64 shows that the distribution of adiabatic effectiveness on the wall is nearly symmetric about the center line of the hole. The magnitude decays in the streamwise direction as the cooled area increases in width.

Figure 65 shows the distribution of adiabatic effectiveness on the wall at the station $X/D = 8.75$ downstream of the hole. This plot shows a symmetric distribution which agrees reasonably with experimental results [66], [65] and [64]. Figure 66 shows the corresponding contours of the instantaneous temperature field at this station.

Figure 67 is the plot of adiabatic effectiveness along the center line downstream of the hole. Very near the hole, the adiabatic effectiveness decreases due to a region of reversed flow. The local minimum was located at $X/D = 0.9$ from the center of the hole. The peak value occurred at $X/D = 3.2$ from the center of the hole. The increase in adiabatic effectiveness results from the reattachment of the flow, which increases the heat transfer at the wall. The peak value of the adiabatic effectiveness for this case with a density ratio of 2.0 and a velocity ratio of 0.5 was 0.78.

79
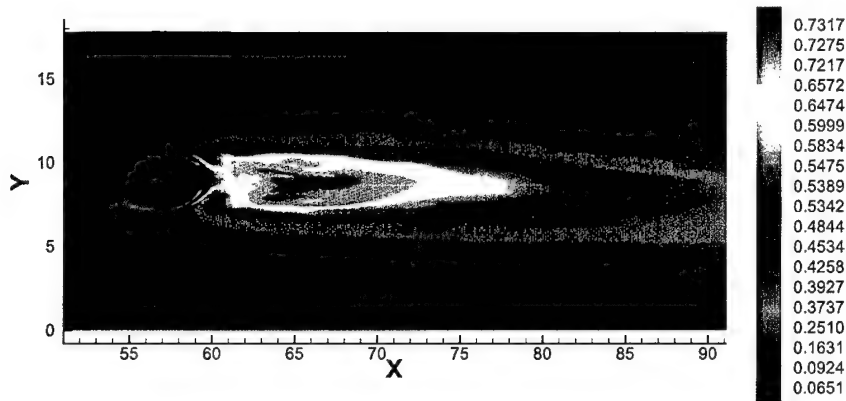
Figure 64: The distribution of adiabatic effectiveness on the flat plate for the case of density ratio $DR = 2.0$, blowing ratio $VR = 0.5$, free stream turbulence level $Tu = 0.0$; X is the streamwise direction and Y is the spanwise direction

The LES results for film cooling look very promising. However, much more remains to be done in order to validate the procedure and apply it to study important issues related to physics and design. The remaining task of highest priority is to make comparisons with experimental results. A case with a density ratio of two was chosen in order to emphasize the power of the compressible LES procedure. Unfortunately, we know of no experimental results for such a large density ratio.

As funding permits, film cooling work that will include the use of shorter supply tubes and a supply plenum in the computational domain will be carried out. Also of considerable interest is the inclusion of significant free stream turbulence. The use of pulsed (unsteady) coolant supply is also of interest.

80
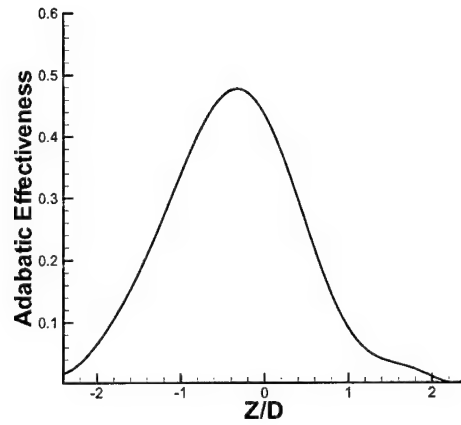
Figure 65: Plot of adiabatic effectiveness at $X/D = 8.75$ downstream of the hole for density ratio $DR = 2.0$, blowing ratio $VR = 0.5$ and free stream turbulence level $Tu = 0.0$

Figure 66: Upstream view of instantaneous temperature contours at $X = 84$ ($X/D = 8.75$); the units of the axes are displacement thickness
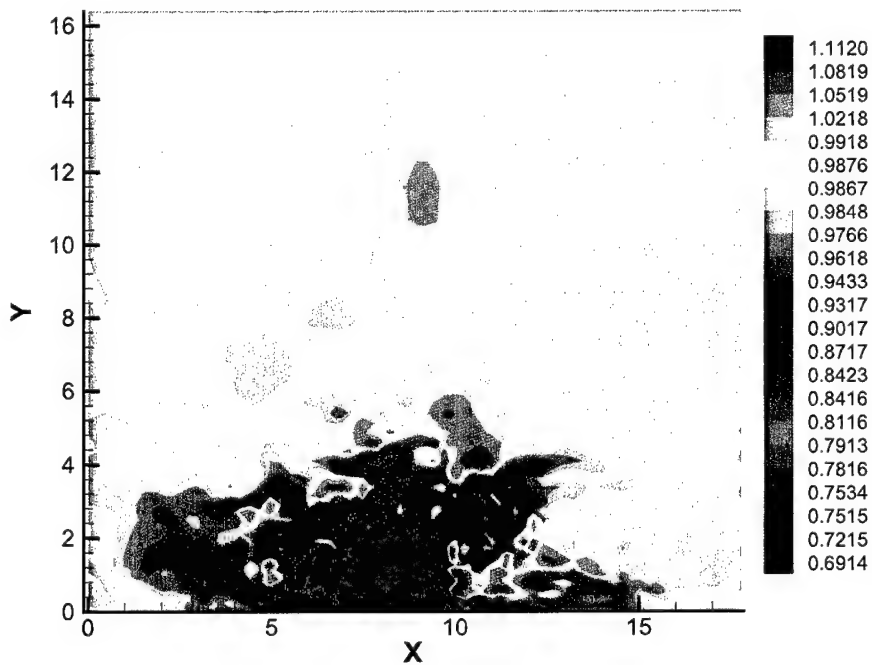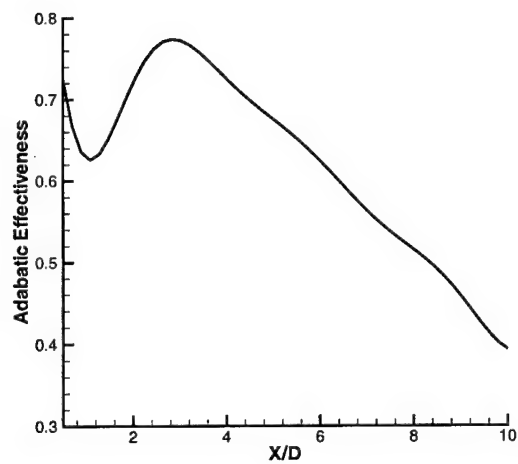
Figure 67: Adiabatic effectiveness along the center line of the flat plate for density ratio $DR = 2.0$, blowing ratio $VR = 0.5$ and free stream turbulence level $Tu = 0.0$

7 Conclusions

Large eddy simulation has been shown to be a very useful tool to aid understanding of the complex flows characteristic of turbine blade cooling systems. At this point the LES technology is limited to relatively low Reynolds numbers and simple geometry, but effects due to rotation and heat transfer can be studied.

The major conclusions from this study are given below.

- Although still somewhat limited to low Reynolds numbers and relatively simple geometries, large eddy simulation was observed to be a valuable tool for examining the behavior of turbulent flows with rotation or rib-roughness that are difficult to compute accurately by other approaches.

- In general, system rotation was found to suppress turbulent velocity fluctuations and shear stresses near the leading side of a rotating channel and enhance them near the trailing side. The ratio of the skin-friction coefficient and Nusselt numbers on the two sides ranged between a factor of 2 and 3. Heat transfer appeared to be influenced somewhat more strongly than skin friction. The maximum mean streamwise velocity was skewed toward the leading side of the rotating channel.

- In the rotating ribbed channel, rotation caused the length of the separated flow region behind the ribs to lengthen on the leading side and shrink on the trailing side. This appears consistent with the observed trend in shear stresses; i.e., increased stresses resulted in more rapid reattachment.

- For a rotating square duct, a distinct secondary flow pattern was observed in the simulations in general agreement with experimental observations. Flow near the sidewalls was driven by the pressure gradient from the trailing side to the leading side and a less intense flow was observed in the central region from the leading side to the trailing side. The latter migration resulted in the maximum in the mean streamwise velocity distribution being shifted toward the trailing side, opposite from the skewing observed in channel flow.

- Centrifugal buoyancy terms were included in the governing equations for the rotating square

83

duct flows with heat transfer. The centrifugal effect was observed to significantly alter the flow pattern. When $Gr < 0$, the buoyancy force was observed to cause flow separation on the leading wall.

- Work was completed toward an efficient fractional step method for solving the compressible Navier-Stokes equations that has some novel features. The scheme was used in the work on external turbulent boundary layers that was necessary for the effort on film cooling.

- A procedure was developed to establish inflow conditions for LES of spatially developing turbulent boundary layers that included the influence of freestream turbulence. This also was part of the film cooling effort.

- A demonstration simulation for an idealized film cooling configuration was completed. The essential components for film cooling simulations are in place and the preliminary results appear reasonable and promising. Work is underway to make quantitative comparisons with experimental data to validate the approach and confirm the level of accuracy.

Acknowledgements

8 Publications

Dissertations that describe research that has been supported wholly or in part by this grant include:

Avancha, R. V. R., "A Study of the Hat Transfer and Fluid Mechanics of the Turbulent Separating and Reattaching Flow Past a Backward Facing Step using Large Eddy Simulation," Ph.D. Dissertation, Iowa State University, 2001.

Lee, J. S., "Large Eddy Simulation of Compressible Turbulent Channel and Annular Pipe Flows with System and Wall Rotations," Ph.D. Dissertation, Iowa State University, 2004.

One Masters thesis described work that was supported by this grant:

Liu, Y., "Large Eddy Simulation of Wall Bounded Turbulent Flows with Heat Transfer," M.S. Thesis, 2002.

Journal articles published that describe research that has been supported wholly or in part by this grant include:

Lee, J. S., Meng, N., Pletcher, R. H. and Liu, Y., "Numerical Study of the Effects of Rotation on Heat Transfer in Channels with and without Ribs," Int. J. Heat and Mass Transfer **47**:4671-4684, 2004.

Dailey, L. D., Meng, N. and Pletcher, R. H., "Large Eddy Simulation of Constant Heat Flux Turbulent Channel Flow with Property Variations: Quasi-Developed Model and Mean Flow Results,"Journal of Heat Transfer **125**: 27-38, 2003.

Avancha, R. V. R. and Pletcher, R. H., "Large Eddy Simulation of the Turbulent Flow Past a Backward-Facing Step with Heat Transfer and Property Variations," Int. J. of Heat and Fluid Flow **23**: 601-614, 2002.

Conference proceedings and preprinted meeting papers that describe research that has been supported wholly or in part by this grant include:

Liu, K. and Pletcher, R. H., "A Procedure to Establish Inflow Conditions for LES of Spatially Developing Turbulent Boundary Layers," ASME Paper HT-FED-2004-56606, paper presented at ASME Heat Transfer/Fluids Engineering Summer Conferences, 2004.

Lee, J. S., Liu, Y. and Pletcher, R. H., "Large Eddy Simulation of the Effects of Rotation on Heat Transfer in a Ribbed Channel," Heet Transfer 2002, Proceedings of the Twelth International Heat Transfer Conference, Elsevier, 2002.

Pletcher, R. H., Lee, J. S., Meng, N. and Avancha, R. 11Parallel Computing: New Power Aids Understanding of Turbulent Flows," Proceedings of the IMECE'02, 2002 ASME International Mechanical Engineering Congress and Expositon, IMECE2002-HT-32818, 2002.

Avancha, R. V. R. and Pletcher, R. H., "Large Eddy Simulation of the Turbulent Flow Past a Backward-Facing Step with Heat Transfer and Property Variations," presented at the Second International Symposium on Turbulence and Shear Flow Phenomena, Stockholm, Sweden, 2001.

Avancha, R. V. R. and Pletcher, R. H., "Large Eddy Simulation of the Turbulent Flow Past a Backward-Facing Step," paper presented at the Third AFOSR International Conference on DNS/LES, Arlington, Texas, 2001.

Meng, N. and Pletcher, R. H., "Large Eddy Simulation of a Rib-Roughened Turbulent Channel Flow with Heat Transfer and Property Variations,"paper presented at the Third AFOSR International Conference on DNS/LES, Arlington, Texas, 2001.

9 Personnel

Professor R. H. Pletcher served as the Principle Investigator throughout the duration of the grant. Graduate student research assistants who participated in the research include Ravikanth Avancha, Yang Liu, Joon Lee, Kunlun Liu, and Zhaohui Qin.

References

[1] Dailey, L. D. and Pletcher, R. H., "Evaluation of Multigrid Acceleration for Preconditioned Time-Accurate Navier-Stokes Algorithms," Computers and Fluids, **25**: 791-811, 1996.

[2] Dailey, L. D., Meng, N. and Pletcher, R. H., "Large Eddy Simulation of Constant Heat Flux Channel Flow with Property Variations: Quasi-developed Model and Mean Flow Results," Journal of Heat Transfer, **125**: 27-38, 2003.

[3] Pletcher ,R. H. and Chen, K.-H., "On Solving the Compressible Navier-Stokes Equations for Unsteady Flows at Low Mach Numbers," AIAA Paper 93-3368-CP, 1993.

[4] Tritton, D. J., "Experiments on Turbulence in Geophysical Fluid Dynamics," Turbulence and Predictability in Geophysical Fluid Dynamics and Climate Dynamics, 172-192, 1985.

[5] Hopfinger, E. J., "Turbulence and Vortices in Rotating Fluids," Theoretical and Applied Mechanics, 117-138, 1989.

[6] Piomelli, U. and Liu, J. H., "Large-Eddy Simulation of Rotating Channel Flows Using a Localized Dynamic Model," Phys. Fluids, **7**: 839-848, 1995.

[7] Moin, P., Squires, K., Cabot, W., and Lee, S., "A Dynamic Subgrid-Scale Model for Compressible Turbulence and Scalar Transport," Phys. Fluids A, **3**: 2746-2757, 1991.

[8] Johnston, J. P., Halleen, H. M., and Lezius, D. K., "Effects of Spanwise Rotation on the Struture of Two-dimensional Fully Developed Turbulent Channel Flow," J. Fluid Mechanics, **56**: 533, 1972.

[9] Han, J. C., Zhang, Y. M., and Lee, C .P., "Influence of Surface Heating Condtion on Local Heat Transfer in a Rotating Square Channel with Smooth Walls and Radial Outward Flow," J. Turbomachinery, **116**: 149-158, 1994.

[10] Kristoffersen, R. and Andersson, I. H., "Direct Simulations of Low-Reynolds-Number Turbulent Flow in Rotating Channel," J. Fluid Mechanics, **256**:163-197, 1993.

[11] Matsubara, M. and Alfreson, P. H., "Experimental Study of Heat and Momentum Transfer in Rotating Channel Flow," Phys. Fluids **8**:2964–2973, 1996.

[12] Han, J. C., Glicksman, L. R., and Rohsenow, W. M., "An Investigation of Heat Transfer and Friction for Rib-Roughened Surfaces," Int. J. Heat Mass Transfer **21**:1143–1155, 1978.

[13] Bergeles, G., and Athanassiadis, N., "The Flow Past a Surface-mounted Obstacle," J. Fluids Engineering, **105**:461–463, 1983.

[14] Sparrow, E. M., and Tao, W. Q., " Enhanced Heat Transfer in a Flat Rectangular Duct with Streamwise-Periodic Disturbaces at One Principal Wall," Trans. ASME J. Heat Transfer **105**, 851–861, 1983.

[15] Drain, L. E., and Martin, S., " Two-component Velocity Measurements of Turbulent Flow in a Ribbed-Wall Flow Channel," Int. Conf. on Laser Anenometry-Advances and Application Manchester, U.K., pp. 99–112, 1985.

[16] Wagner, J. H., Johnson, B. V., Graziani, R. A., and Yeh, F. C., "Heat Transfer in Rotating Serpentine Passages with Trips Normal to the Flow," J. Turbomachinery **114**:847–857, 1992.

[17] Vreman, B., Geurts, B., and Kuerten, H., "Subgrid-Modeling in LES of Compressible Flow," Applied Scientific Research, **54**:191-203, 1995.

[18] Dailey, L. D. and Pletcher, R. H., "Evaluation of Multigrid Acceleration for Preconditioned Time-accurate Navier-Stokes Algorithms," Computers & Fluids, **25**:791-811, 1996.

[19] Germano, M., "Turbulence: the Filtering Approach," J. Fluid Mechanics, **238**:325–336, 1992.

[20] Huang, P. G., Coleman, G. N., and Bradshaw, P., "Compressible Turbulent Channel Flow - a Close Look Using DNS Data," AIAA Paper, 95-0584, 1995.

[21] Favre, A., "Turbulence: Space-time Statistical Properties and Behavior in Supersonic Flows," Physics of Fluids, **26**: 2851-2863, 1983.

[22] Cebeci, T. and Smith, A. M. O., Analysis of Turbulent Boundary Layers, Academic Press, New York, 1974.

[23] Lilly, D. K., "A Proposed Modification of the Germano Subgrid-scale Closure Method," Physics of Fluids A, **4**: 633-635, 1992.

[24] Rieger, H. and Jameson, A., "Solution of Steady Three-Dimensional Compressible Euler and Navier-Stokes Equations by an Implicit LU Scheme," AIAA Paper 88-0619, 1988.

[25] Thompson, K. W., "Time Dependent Boundary Conditions for Hyperbolic Systems. No.1," J. of Comp. Phys., **68**:1–24, 1987.

[26] Thompson, K. W., "Time Dependent Boundary Conditions for Hyperbolic Systems. No.2," J. of Comp. Phys., **89**:439–461, 1990.

[27] Poinsot, T. J. and Lele, S. K., "Boundary Conditions for Direct Simulations of Compressible Viscous Flow," J. of Comp. Phys., **101**:104–129, 1992.

[28] Rudy, D. H. and Strikwerda, J. C., " Boundary Conditions for Subsonic Compressible Navier-Stokes Calculations," Computers & Fluids, **9**:327–338, 1981.

[29] Huser, A. and Biringen, S., "Direct Numerical Simulation of Turbulent Flow in a Square Duct," J. Fluid Mechanics, **257**:65–95, 1993.

[30] Cheesewright, R., McGrath, G. and Petty, D. G., " LDA Measurements of Turbulent Flow in a Duct of Square Cross Section at Low Reynolds Number," Aeronautical Engineering Dept. Rep. ER 1011., Queen Mary Westfield College. University of London, 1990.

[31] Balint, J.-L., Wallace, J. M. and Vukoslavcevic, P., " The Velocity and Vorticity Vector Fields of a Turbulent Boundary Layer. Part 2. Statistical Properties," J. Fluid Mechanics, **228**:53–86, 1991.

[32] Vazquez, M. S. and Metais, O., "Large-Eddy Simulation of the Turbulent Flow Through a Heated Square Duct," J. Fluid Mechanics, **453**:201–238, 2002.

[33] Pallares, J. and Davidson, L., "Large-Eddy Simulations of Turbulent Heat Transfer in Stationary and Rotating Square Ducts," Phys. Fluids, **14**:2804–2816, 2002.

[34] Brundrett, E. and Burroughs, P. R., "The Temperature Inner Law and Heat Transfer for Turbulent Air Flow in a Vertical Square Duct," Int. J. Heat Mass Transfer, **10**:1133–1142, 1967.

[35] Kim, J., Moin, P. and Moser, R., "Turbulence Statistics in Fully Developed Channel Flow at Low Reynolds Number," J. Fluid Mechanics, **177**:133–166, 1987.

[36] Kim, J., Moin, P., "Transport of Passive Scalars in a Turbulent Channel Flow," Turbulent Shear Flows 6, Springer-Verlag, 85–96, 1989.

[37] Kong, H., Choi, H. and Lee, J. S., "Direct Numerical Simulation of Turbulent Thermal Boundary Layers," Phys. Fluids, 12: 2555–2568, 2000.

[38] Kasagi, N., Kuroda, A. and Hirata, M., "Numerical Investigation of Near-Wall Turbulent Heat Transfer Taking into Account the Unsteady Heat Conduction in the Solid Wall," J. Heat Transfer, 111:385–392, 1989.

[39] Kays, W. M. and Crawford, M. E., Convective Heat and Mass Transfer," 3rd edition, McGraw-Hill, 1993.

[40] Sparrow, E. M., Garcia, A. and Chuck, W., "Numerical and Experimental Turbulent Heat Transfer Results for a One-Sided Heated Rectangular Duct," Numerical Heat Transfer, 9:301–322, 1986.

[41] Wardana, I. N. G., Ueda, T. and Mizomoto, T., "Effect of Strong Wall Heating on Turbulence Statistics of a Channel Flow," Exps. Fluids, 18:87–94, 1994.

[42] Gavrilakis, S., "Direct Numerical Simulation of Turbulent Flow in Rotating Flow Through a Straight Square Duct," Private Communication.

[43] Murata, A. and Mochizuki, S., "Effect of Cross-Sectional Aspect Ratio on Turbulent Heat Transfer in an Orthogonally Rotating Rectangular Smooth Duct," Int. J. Heat Mass Transfer, 42:3803–3814, 1999.

[44] Han, J. C. and Zhang, Y. M., "Effect of Uneven Wall Temperature on Local Heat Transfer in a Rotating Square Channel with Smooth Walls and Radial Outward Flow," J. of Heat Transfer, 114:850–858, 1992.

[45] Han, J. C., Zhang, Y. M. and Kalkuehler, K., "Uneven Wall Temperature Effect on Local Heat Transfer in a Rotating Two-Pass Square Channel with Smooth Walls," J. of Heat Transfer, 115:912–920, 1993.

[46] Hwang, J. J., Lia, T. Y. and Chen, S. H., "Prediction of Turbulent Fluid Flow and Heat Transfer in a Rotating Periodical Two-Pass Square Duct," Int. J. Numerical Methods for Heat and Fluid Flow, **8**:519–538, 1998.

[47] Kim, J., Moin, P., "Application of a Fractional Step Method to Incompressible Flows," J. Comput. Phys. **59**: 308-323, 1985.

[48] Dennis, J. E. and Schnabel, R. B., Numerical Methods for Unconstrained Optimization and Nonlinear Equations, SIAM, Philadelphis, 1996.

[49] Choi, H. and Moin, P. "Effects of the Computational Time Step on Numerical Solutions of Turbulent Flow,", J. Comput. Phys., **113**: 1-14, 1994.

[50] Perot, J. B.," An Analysis of the Fractional Step Method," J. Comput. Phys.,**108**: 51, 1993.

[51] Liu, K. and Pletcher, R. H., " A Procedure to Establish Inflow Conditions for LES of Spatially Developing Turbulent Boundary Layers," ASME Heat Transfer/Fluids Engineering Summer Conferences, HT-FED04-56606, 2004.

[52] Spalart, P. R., "Direct Numerical Simulation of Turbulent Boundary Layer up to $R_{theta} = 1410$," J. Fluid Mech. **187**: 61-98 (1988).

[53] Lund, T. S., Wu, X. and Squires, K. D., "Generation of Turbulent Inflow Data for Spatially-Developing Boundary Layer Simulation," J. Comput. Phys., **140**: 233-258, 1998.

[54] Spille-Kohoff, A., and Kaltenbach, H.-J., "Generation of Turbulent Inflow Data with a Pre-scribed Shear-Stress Profile," Third AFOSR Conf., Arlington, Texas, 319-326, 2001.

[55] Simonich, J. C. and Bradshaw, P., "Influence of Free-Stream Turbulence on Turbulent Boundary Layer Heat Transfer and Mean Profile Development, Part II-Analysis of Results," J. Heat Transfer, **105**: 41-53, 1983.

[56] Hancock, P. E. and Bradshaw, P., "Effect of Free-Stream Turbulence on Turbulent Boundary Layers," J. Fluids Eng., **105**: 284-289, 1983.

[57] Barrett, M. J. and Hollingsworth, D. K., "On the Calculation of Length Scales for Turbulent Heat Transfer Correlation," J. Heat Transfer, **123** : 878-883, 2001.

[58] Barrett, M. J. and Hollingsworth, D. K., "Heat Transfer in Turbulent Boundary Layers Subjected to Free-stream Turbulence, Part I: Experimental Results," J. Turbomachinery, **125**: 232-241, 2003.

[59] Cebeci,T. and Bradshaw, P., Momentum Transfer in Boundary Layers, Hemisphere, 1977.

[60] DeGraaff, D. B. and Eaton, J. K., "Reynolds-Number Scaling of the Flat-Plate Turbulent Boundary Layer," J. Fluid Mech. **422**:319-346, 2000.

[61] Germano, M., Piomelli, U., Moin, P. and Cabot, W. H., "A Dynamic Subgrid-Scaled Eddy Viscosity Model," Phys. of Fluids, **A 3**: 1760-1765, 1991.

[62] Barrett, M. J. and Hollingsworth, D. K., "Correlation Friction Velocity in Turbulent Boundary Layers Subjected to Freestream Turbulence," AIAA J., **41**:1444-1451, 2003.

[63] Goldstein, R. J., Eckert, E. R. G., and Burggraf, F., "Effects of Hole Geometry and Density on Three-Dimensional Film Cooling,"Int. J. Heat Mass Transfer: **17**: 595-607, 1974.

[64] Burd, S. W., Kaszeta, R. W., and Simon, T. W. "Measurements in Film Cooling Flows: Hole L/D and Turbulence Intensity Effects,"ASME. 96-WA/HT-7, 1996.

[65] Ligrani P. M. , Wigle J. M. and Jackson S. M., "Film-Cooling from Holes with Compound Angle Orientations: Part 2-Results Downstream of Two Staggered Rows of Holes with 6D Spanwise Spacing,"J. Heat Transfer: **116**: 353-362, 1994.

[66] Ligrani P. M. , Wigle J. M. , Ciriello S. and Jackson S. M. , "Film-Cooling from holes with compound angle orientations: Part 1-Results Downstream of Two Staggered Rows of Holes with 3D Spanwise Spacing,", J. Heat Transfer: **116**: 341-352, 1994.